Economic Geology, v. 119, no. 5, pp. 1059–1087

Contrasting Tectonomagmatic Conditions for Coexisting Iron Oxide-Apatite Deposits and Porphyry and Skarn Cu ± Au Deposits in the Middle-Lower Yangtze River Metallogenic Belt, China

Xuyang Meng,[1,2,†] Jingwen Mao,[1,3] Adam Simon,[2] Chao Duan,[3] Guiqing Xie,[1,3] Huimin Su,[4] Tong Hou,[1] Ke Shi,[5] and Nian Chen[1]

[1] *MNR Key Laboratory for Exploration Theory and Technology of Critical Mineral Resources, School of Earth Sciences and Resources, China University of Geosciences, Beijing 100083, China*

[2] *Department of Earth and Environmental Sciences, University of Michigan, Ann Arbor, Michigan 48109, USA*

[3] *MNR Key Laboratory of Metallogeny and Mineral Assessment, Institute of Mineral Resources, Chinese Academy of Geological Sciences (CAGS), Beijing 100037, China*

[4] *Collaborative Innovation Center for Exploration of Strategic Mineral Resources, China University of Geosciences, Wuhan 430074, China*

[5] *MNR Innovative Center of Coverage Area Deep Resource Exploration Engineering Technology, Geological Survey of Anhui Province, Hefei 230001, China*

Abstract

Porphyry Cu ± Mo ± Au and iron oxide-apatite (IOA) deposits rarely occur in spatial and temporal proximity in Phanerozoic arc-related settings, and the formation of these mineral deposit types in an evolving arc setting remains poorly understood. Specifically, the roles of magma composition and the tectonic regime remain the subject of some debate. Here, we systematically estimated the P-T-f_{O_2} conditions and H_2O-S-Cl contents for dioritic to granodioritic source magmas for porphyry and skarn Cu ± Au (150–135 Ma) and IOA deposits (~130 Ma) that formed in transpressional and transtensional settings in the Middle-Lower Yangtze River metallogenic belt, China. Our estimates show that, compared to IOA deposits, the porphyry- and skarn-related magmas were relatively felsic, cooler, and more hydrous. These geochemical features are consistent with the tectonic transition from subduction to slab rollback of the paleo-Pacific plate in the East Asia continental margin at <135 Ma and concomitant crustal extension and steepening of the regional geothermal gradient.

Apatite data reveal that the silicate melts associated with the porphyry and skarn Cu ± Au and IOA deposits had comparable predegassed S concentrations (~0.13 ± 0.06 wt % vs. ~0.16 ± 0.09 wt % on average), but that IOA-related melts contained higher predegassed Cl/H_2O ratios (~0.11 ± 0.03 vs. ~0.04 ± 0.03 for porphyry- and skarn-related magmas) that decreased by one order of magnitude after magmatic degassing. Magmatic f_{O_2} estimated using zircon and amphibole, reported in log units relative to the fayalite-magnetite-quartz (FMQ) redox buffer, gradually increased during cooling of the porphyry- and skarn-related magmas (ΔFMQ +0.7 to +2.5) at 950° to 800°C and decreased to ΔFMQ +1 at 700°C owing to fractionation of Fe^{2+}-rich minerals and subsequent S degassing, respectively. In contrast, the magmatic f_{O_2} values for the IOA-related source magmas varied significantly from ΔFMQ –1.5 to ΔFMQ +2.5 but generally show an increasing trend with cooling from 970° to 700°C that probably resulted from variable degrees of evaporite assimilation, fractionation of Fe^{2+}-rich minerals, and Cl degassing. These results are consistent with the hypothesis that Cl enrichment of the IOA-related source magmas played a determinant role in their formation.

We propose that the porphyry and skarn Cu ± Au deposits in the Middle-Lower Yangtze River metallogenic belt formed in a transpressional setting in response to paleo-Pacific flat-slab subduction that favored storage and evolution of S-rich hydrous ore-forming magmas at variable crustal levels. A subsequent extensional setting formed due to slab rollback, leading to rapid degassing of Cl-rich IOA-related magmas. For the latter scenario, assimilation of evaporite by mafic to intermediate magmas would lead to an enrichment of Cl in the predegassed magmas and subsequent exsolution of hypersaline magmatic-hydrothermal fluid enriched in Fe as $FeCl_2$. This Fe-rich ore fluid efficiently transported Fe to the apical parts of the magma bodies and overlying extensional normal faults where IOA mineralization was localized. The concomitant loss of S, H_2O, and Cu with Cl by volcanic outgassing may have inhibited sulfide mineralization at lower temperatures.

Introduction

Porphyry Cu ± Au ± Mo deposits (hereafter simply "porphyry Cu deposits") are the greatest sources of Cu and Mo and supply significant Au, Ag, and metals such as Te (Sillitoe, 2003, 2010; Cooke et al., 2005, 2014; Richards and Mumin, 2013a, b; Kesler and Simon, 2015). Iron oxide-apatite (IOA) deposits are important sources of iron and phosphates and have the potential to supply significant rare earth elements (REEs) hosted in apatite (Barton, 2013; Simon et al., 2018; Troll et al., 2019; Reich et al., 2022). Porphyry Cu deposits typically form in compressional to transpressional settings of crustal-thickening convergent margins (Richards, 2003; Sillitoe, 2010; Meng et al., 2021a, b, 2022), whereas IOA deposits commonly form under extensional to transtensional back-arc settings

†Corresponding author: e-mail, xmeng1@cugb.edu.cn

ISSN 0361-0128; doi:10.5382/econgeo.5084; 29 p.
Digital appendices are available in the online Supplements section.

Submitted: March 26, 2023/Accepted: January 23, 2024

(Sillitoe, 2003; Groves et al., 2005, 2010; Mao et al., 2011; Barton, 2013; Richards and Mumin, 2013a, b; Reich et al., 2022; Skirrow, 2022). While it is well documented that porphyry Cu and IOA deposits are not genetically related, both mineral deposit types are observed to have occurred in spatial and temporal proximity in the Mesozoic Coastal Cordillera of northern Chile and southern Peru (Sillitoe, 2003; Richards et al., 2017) and Middle-Lower Yangtze river belt in China (Mao et al., 2011; Zhou et al., 2013).

The parental magmas for the magmatic-hydrothermal ore fluids that form porphyry Cu and IOA deposits are generally thought to be derived from partial melting of metasomatized mantle lithosphere (Richards, 2003; Groves et al., 2010). The observation that IOA deposits contain much less Cu-Fe sulfide ore relative to porphyry Cu deposits has been interpreted to indicate that their source magmas were S poor (Richards and Mumin, 2013a, b). This hypothesis can explain the preferential occurrence of IOA versus porphyry Cu deposits in extensional back-arc settings, because magmas formed during asthenospheric upwelling may be S poor owing to the subdued contribution of oxidized sulfur from the subducting slab to the mantle (Richards et al., 2017). However, it remains unclear as to whether and how contrasting tectonomagmatic conditions controlled the formation of these two distinct mineral systems in an evolving arc setting.

To better understand the spatiotemporal relationship among porphyry Cu and IOA deposits, we systematically investigated intrusive rocks for the P-T-f_{O_2} conditions and S-Cl concentrations of the source magmas related to representative well-characterized porphyry and skarn Cu ± Au and IOA deposits in the Middle-Lower Yangtze River metallogenic belt. In comparison to the Coastal Cordillera of northern Chile and Peru, the belt only comprises IOA deposits with minor, noneconomic Cu-Fe sulfide mineralization (Table 1). These new belt-scale data sets are interpreted in a geologic background to reflect the fundamental tectonic and magmatic control on the two types of mineralization in the Middle-Lower Yangtze River metallogenic belt. A combination of differences in magmatic P-T-f_{O_2} conditions and volatile compositions is proposed here to have favored the formation of porphyry and skarn Cu ± Au and IOA deposits under broadly compressional and extensional arc settings in the metallogenic belt, respectively. Evaporite assimilation is suggested to be a key external trigger for IOA deposit formation.

Tectonic, Magmatic, and Metallogenic Settings of the Mesozoic Middle-Lower Yangtze River Metallogenic Belt

The arcuate-shaped Middle-Lower Yangtze River metallogenic belt hosts ~200 polymetallic deposits and has a lateral extent of approximately ~550 km along the Yangtze River at the northeastern margin of the Yangtze craton in eastern China (Fig. 1; Chang et al., 1991; Zhai et al., 1992; Pan and Dong, 1999; Mao et al., 2011). A total indicated and measured metal resource of 13.9 million tonnes (Mt) Cu, >600 t Au, and 2.49 billion tonnes (Bt) Fe has been defined (Zhao et al., 1999; Yin et al., 2016). It is bound to the north by the Dabie orogen and North China craton along the Xiangfan-Guangji and Tancheng-Lujiang faults and to the south by the Yangtze craton along the Yangxin-Changzhou fault (Chang et al., 1991; Zhai et al., 1992). The Precambrian crystalline basement in the Middle-Lower Yangtze River metallogenic belt mainly includes metamorphosed late Archean to Paleoproterozoic tonalite-trondhjemite-granodiorite rocks. This contrasts with the crystalline basement of Neoproterozoic metamorphosed flysh-like clastic sedimentary sequences in the south Yangtze craton (Fig. 1; Qiu et al., 2000; Dong et al., 2011).

The crystalline basement rocks in the Middle-Lower Yantze River metallogenic belt are overlain by Paleoproterozoic to Neoproterozoic (1850–990 Ma) volcanosedimentary and Paleozoic-Early Triassic clastic and dolomitic successions, including siltstone, shale, and limestone (Chang et al., 1991). Extensive fault networks developed during the Neoproterozoic Jiangnan orogeny due to subduction-related collision of the Cathaysia terrane and Yangtze craton (Yao et al., 2014; Goldfarb et al., 2021). Shallow marine carbonate and evaporite sequences deposited in the Triassic are unconformably overlain by late Triassic-Jurassic terrestrial coal, sandstone, and mudstone (Chang et al., 1991; Zhai et al., 1992).

Plate reconstruction shows that the paleo-Pacific oceanic plate has subducted beneath the Eurasian plate (Fig. 2a) since the early Jurassic (Li et al., 2019); this may be flat or low-angle subduction (Li and Li, 2007; Wu et al., 2019; Liu et al., 2021; Qiu et al., 2023). The velocity of the paleo-Pacific plate is suggested to have steadily increased from ~155 to 137 Ma, and then decreased abruptly after ~135 Ma (Fig. 2b). Although the geodynamic setting for forming the Middle-Lower Yangtze River metallogenic belt remains debated (Table 1), the change in the plate velocity is consistent with the evolving kinematic regime in the belt that changed from transpression prior to ~135 Ma to strike-slip extension from 135 to 127 Ma, and then to purely extension at ~126 to 123 Ma (Chang et al., 2012), consistent with the evolving tectonic framework of the East Asian continental margin (Li, J., et al., 2014; Zhou et al., 2015; Li et al., 2019). Chen et al. (2020) noted a slight northeastward migration of the high-K calc-alkaline mafic magmatism in the Middle-Lower Yangtze River metallogenic belt and interpreted this as the manifestation of local extension caused by slab rollback beginning around 140 Ma. However, the compiled geochronological data suggest the age variation of high-K calc-alkaline magmatism across the Middle-Lower Yangtze River metallogenic belt is exceptionally limited (Fig. 3). Lithospheric extension is supported by decreasing crustal thickness in the Middle-Lower Yangtze River metallogenic belt from 62 ± 6 km (1σ, n = 254) to 49 ± 8 km from ~150 to 135 Ma to <133 Ma (1σ, n = 40; Fig. 2c), which was estimated using published whole-rock La/Yb ratios following the method of Profeta et al. (2015). Extension likely commenced at ~140 Ma, but was not widespread until ~135 Ma in response to eastward retreating subduction of the paleo-Pacific oceanic plate, rollback of a steeper slab, upwelling of asthenospheric mantle, and/or lithospheric delamination at the East Asian continental margin (Zhu and Xu, 2019; Zhang et al., 2020; Lü et al., 2021; Mao et al., 2021).

The subduction of the paleo-Pacific oceanic plate and the subsequent rollback or retreating produced voluminous dioritic to granodioritic magmas in the Jurassic to Early Cretaceous that intruded sedimentary sequences in the Middle-Lower Yangtze River metallogenic belt along reactivated basement-penetrating faults (Pan and Dong, 1999; Mao et al., 2011; Yang

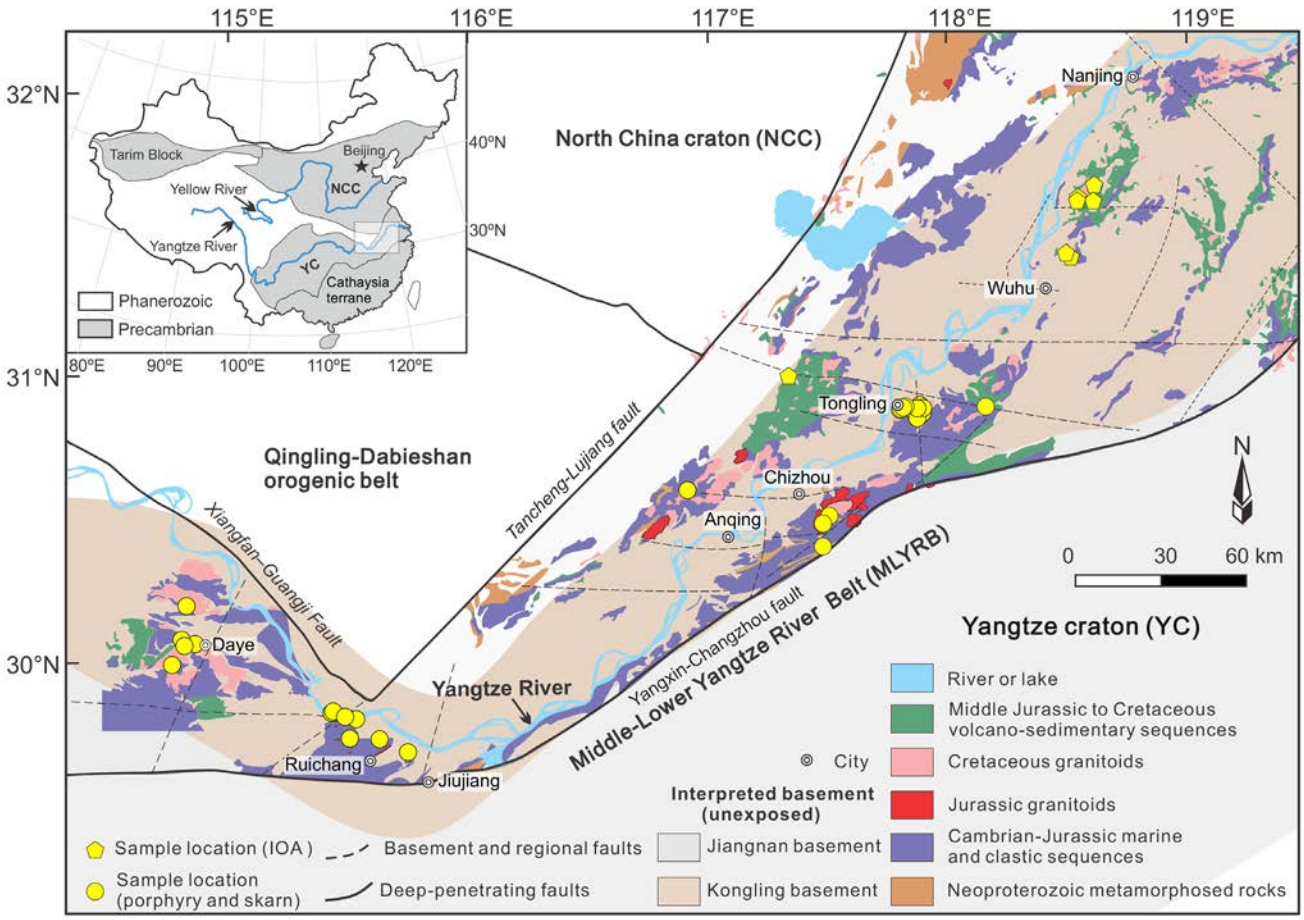

Fig. 1. Simplified geologic map for the Middle-Lower Yangtze River metallogenic belt, modified from Mao et al. (2017). Inset map shows the location of the belt in mainland China, modified from Zheng et al. (2013). The distribution of the crystalline basements are approximated following Dong et al. (2011). The distribution of the crystalline basements is projected to surface; they are not well exposed like the map shows. IOA = iron oxide-apatite.

and Cooke, 2019). The Jurassic-Cretaceous magmatism in the belt occurred in three episodes (Mao et al., 2011; Zhou et al., 2013; Chen et al., 2020): (1) ~152 to 135 Ma high-K calc-alkaline I-type granitoid associated with porphyry and skarn Cu ± Au deposits (Figs. 2b, 3), (2) ~133 to 125 Ma shoshonitic intrusive and volcanic sequences associated with IOA deposits (Figs. 2b, 3), and (3) slightly younger A-type intrusive rocks with granitic–syenitic compositions (<130 Ma) associated with subeconomic Au mineralization. The porphyry and skarn Cu ± Au and IOA deposits mainly formed at broadly transpressional (or in transition to transtension) and transtensional settings at ~140 and ~130 Ma, respectively (Fig. 2b).

Jurassic to early Cretaceous ore deposits

These mineral deposits have been grouped into seven discrete ore districts from west to east, including Edong, Jiujiang-Ruichang (Jiurui), Anqing-Guichi, Tongling, Lujiang-Zongyang (Luzong), Nanjing-Wuhu (Ningwu), and Nanjing-Zhenjiang (Ningzhen; Fig. 1; Mao et al., 2011; Pirajno and Zhou, 2015). The porphyry and skarn Cu ± Au deposits are mainly clustered in Daye, Jiurui, Anqing-Guichi, and Tongling (i.e., at latitude of 29.5°E–31°E), whereas the IOA deposits are restricted to the northeastern part of the belt (Fig. 3), including the Ningwu (Nanjing-Wuhu) and Luzong (Lujiang-Zongyang) ore districts (Fig. 1). A few skarn Fe deposits have also been reported in the Edong and Luzong ore districts, which mainly formed at the same time as the IOA deposits (Fig. 3). The porphyry and skarn Cu ± Au deposits of the Middle-Lower Yangtze River metallogenic belt are genetically associated with granodioritic to quartz dioritic stocks that were emplaced into thick carbonate and clastic sedimentary sequences. The contrasting alteration features of the porphyry and skarn Cu ± Au deposits are mainly affected by host rocks (clastic versus carbonate; Table 1). Massive, disseminated, and veinlet mineralization are primarily hosted in skarns along the contacts between the intrusions and the carbonate sequences or are stratabound between the limestone-dolomite sequences (Tables 1, 2). Mineralization is also hosted in quartz dioritic to granodioritic stocks with potassic and phyllic alteration in Tongshankou, Baoshan, Chengmenshan, Wushan, Matou, and Dongguashan where the hosts are clastic rocks (Table 2).

The Middle-Lower Yangtze River metallogenic belt IOA deposits are spatially and temporally associated with synvolcanic gabbroic to dioritic intrusions emplaced in the Early Cretaceous volcanic basins or Triassic sedimentary sequences (Mao et al., 2011; Zhao et al., 2020). Mineralization styles include massive, breccia-hosted dissemination and veinlets that occur in the apical parts of the dioritic intrusions or at their

Table 1. Summary of Previous Studies on Main Mineral Deposits in Middle-Lower Yangtze River Metallogenic Belt (MLYRMB), China

	Porphyry and skarn Cu-Au deposits	Iron oxide-apatite deposits
Ages	152–135 Ma (~140 Ma)	135–126 Ma (~130 Ma)
Kinematic regime	Transpression (Chang et al., 1991, 2012; Mao et al., 2006)	Transtension (Chang et al., 1991, 2012; Mao et al., 2006)
Ore tonnage	13.9 Mt Cu and >600 t Au (Yin et al., 2016; Zhao et al., 1999)	2.49 Bt Fe (Yin et al., 2016)
Ore-forming magmas	High-K calc-alkaline diorite, quartz diorite, and granodiorite	Shoshonitic diorite porphyry
Host rocks	Clastic sedimentary rocks (e.g., sandstone) and carbonates (e.g., limestone, dolomite)	(1) Coeval early Cretaceous andesite and tuffs; (2) shale, calcareous siltstone, and mudstone, quartz sandstone, and conglomerate
Alteration	Qtz ± Kfs ± Bt, Qtz ± Ser, Grt ± Di ± Act ± Chl ± Ep ± Serp, Qtz ± Cal	Ab ± Phl ± Act ± Ap, Di ± Anh ± Grt ± Ap
Mineralization	Disseminated, veinlet, and/or massive Ccp ± Py ± Mt (± Po in skarn) mineralization	Disseminated, massive, and breccia-hosted Mt mineralization
Nature of ore fluids	Moderate to high temperature (~600–200 °C) magmatic-hydrothermal saline, CO_2-bearing fluids exsolved from the magma chamber, probably being interacted with meterioic water during late stages of mineralization (Chen and Li, 2009; Zhou et al., 2015; Cao et al, 2017)	High to moderate temperature (~800–250 °C; ~700–400 °C for main magnetite deposition) magmatic-hydrothermal S-rich saline fluids (up to ~90 wt. % $NaCl_{equiv}$) subsequently mixed with meteoritic water (Li, W., et al., 2015; Luo et al., 2015); liquid immiscibility model triggered by minor addition of P by crustal assimilation has also been proposed (Hou, T., et al., 2011)
Sources for metal	Copper and Au are mainly sourced from the hydrothermal fluids exsolved from the magma chamber, whereas the sulfur for some of these deposits are from magmatic fluids assimilated by minor evaporite sequence (Hou, Z.Q., et al., 2011; Mao et al., 2011; Zhou et al., 2013)	Derivation of iron mainly from magmatic fluids exsolved from the magma chamber (Mao et al., 2011; Zhou et al., 2013; Zhao et al., 2020); sulfur is mainly from assimilation of evaporite sequences as evidenced by the high $\delta^{34}S$ ratios, possibly upon emplacement of the magmas (Duan et al., 2021)
Magmatic origin	Delamination or partial melting of the thickened ancient lower continental crust (Wang et al., 2007; Hou, Z.Q., et al., 2011); or interaction of crustal materials with magmas derived from metasomatized mantle source regions (Li et al., 2008; Mao et al., 2011; Chen et al., 2020; Yan et al., 2021)	Remelting of the subduction-modified lithospheric mantle with possible assimilation of evaporite sequences during magma emplacement at shallow levels (Fan et al., 2019)
Geophysical feature	(1) Low-velocity zone observed in the uppermost mantle at 100–200 km beneath the MLYRMB via ambient noise and teleseismic approaches, which is interpreted to represent a hot upper mantle that was partially molten resulting from partial melting of the Paleo-pacific plate or mantle source induced by the westward subduction of the paleo-Pacific plate (Ouyang et al., 2014) (2) A summary of seismic and magnetotelluric surveys suggests an anomalously thin lithosphere, low S- and P-wave seismic velocity, and a dipping high-conductivity body extending from the lower crust to the asthenosphere, which are interpreted to be affected by delamination and asthenospheric upwelling during Late Mesozoic (Lü et al., 2021 and references therein); this is consistent with the crustal thinning since <135 Ma observed in this and previous studies	
Geodynamic setting	Model 1 (Subduction-related): Ore-forming magmas derived from partial melting of metasomatized subcontinental lithospheric mantle by fluids released during dehydration or partial melting of the subducting paleo-Pacific or Izanagi slab (e.g., flat slab, slab ridge, or teared slab) at >135 Ma (Ling et al., 2009; Mao et al., 2011; Wu et al., 2012; Ouyang et al., 2014; Wang, F.Y., et al., 2014; Yang et al., 2014b; Pirajno and Zhou, 2015; Gu et al., 2018; Yan et al., 2021; Zhang, J., et al., 2021); slab roll-back is debated to have occurred between 150 Ma and 135 Ma (Yang et al., 2014a; Chen et al., 2020) Model 2 (Intraplate): Ore-forming magmas formed in a setting of delamination of enriched lithospheric mantle or lower crust, as well as asthenospheric upwelling (Wang et al., 2007; Li et al., 2008; Hou, Z.Q., et al., 2011; Zhou et al., 2015; Yang and Cooke, 2019), in response to weakening of compressive stress during (1) a shift from Tethysian to paleo-Pacific plate subduction since late Jurassic or (2) the change in subduction direction or rollback of paleo-Pacific plate after ~135 Ma (Zhou et al., 2015; Chen et al., 2020)	Model 1: Lithospheric extension in response to changes in the motion of Izanagi plate parallel to East Eurasian continental margin, slab rollback and destabilization of the thickened enriched lithospheric mantle and lower crust (Wang et al., 2006; Mao et al., 2011; Zhou et al., 2013; Wang, F.Y., et al., 2014; Chen et al., 2020) Model 2: Upwelling of asthenosphere mantle break the stagnant paleo-Pacific flat slab and make mafic melts underplated at the crust (Pirajno and Zhou, 2015)

Abbreviations: Ab = albite, Act = Actinolite, Ap = apatite, Anh = anhydrite, Bt = biotite, Cal = calcite, Ccp = chalcopyrite, Chl = chlorite, Di = diopside, Ep = epidote, Grt = garnet, Kfs = K-feldspar, Mt = magnetite, Phl = phlogopite, Po = pyrrhotite, Qtz = quartz, Ser = sericite

contacts with the carbonate sequences, where skarns have formed (Tables 1, 2). High-temperature sodic alteration was followed by ore-stage actinolite ± apatite ± diopside ± chlorite ± epidote alteration and sulfide (pyrite + chalcopyrite) ± sulfate (gypsum + anhydrite) veins (Zhou et al., 2013; Duan et al., 2021). Representative IOA deposits include Washan, Gaocun, Heshangqiao, Baixiangshan, and Zhongjiu-Gushan in the Ningwu basin and the Nihe deposit in the Luzong basin. Magnetite from the massive and vein ores in the Washan and Gaocun deposits has been estimated to crystallize at temperatures of 550° to 800°C, consistent with mineralization temperature for IOA deposits worldwide (Zeng et al., 2022). The iron ores

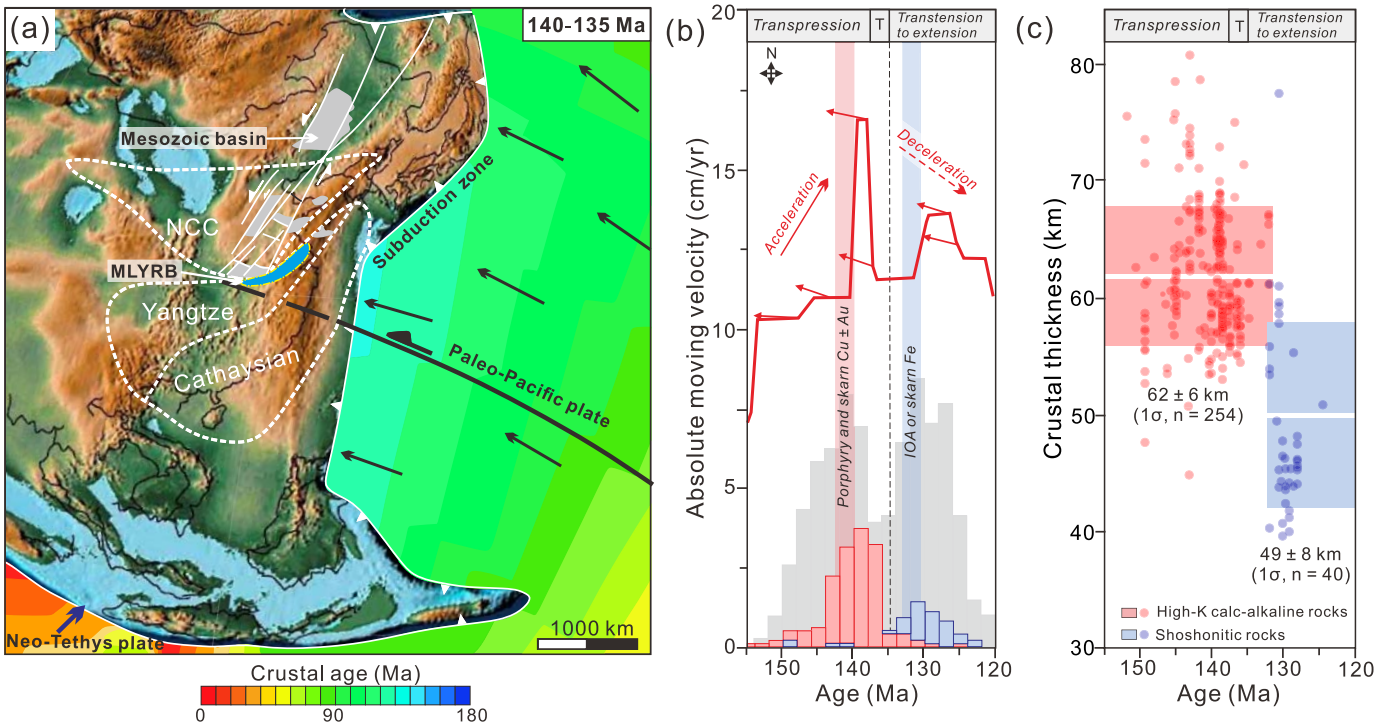

Fig. 2. (a) Plate reconstruction in the east Asian continent and the paleo-Pacific Ocean at 140 to 135 Ma (modified from Li et al., 2019). (b) Change in the velocity of paleo-Pacific plate during 155 to 120 Ma with the histogram for age of magmatism (in gray, n = 790) that is overlain by the stacked histograms for formation ages of porphyry and skarn Cu ± Au and iron oxide-apatite [IOA] deposits (in pink and blue; n = 151 and 48, respectively). (c) Plot of crustal thickness versus age of the igneous rock samples in the Middle-Lower Yangtze River metallogenic belt (MLYRB). See the compiled data set for the ages of magmatism and mineralization in Appendix Tables A5 and A6. The interpretated kinematic regime in panels (b) and (c) is from Chang et al. (2012). T represents "transitional" in panels (b) and (c). The crustal thicknesses are estimated using previously published whole-rock La/Yb ratios (Profeta et al., 2015); the whole-rock geochemistry data have been compiled in Chen et al. (2020) and are filtered using criteria as follows: (1) SiO_2 = 55 to 68 wt %, (2) MgO = 1 to 6 wt %, (3) loss on ignition (LOI) < 2.5 wt %, and (4) Rb/Sr ratio = 0.05 to 0.20. N represents the number of data points. NCC = North China craton.

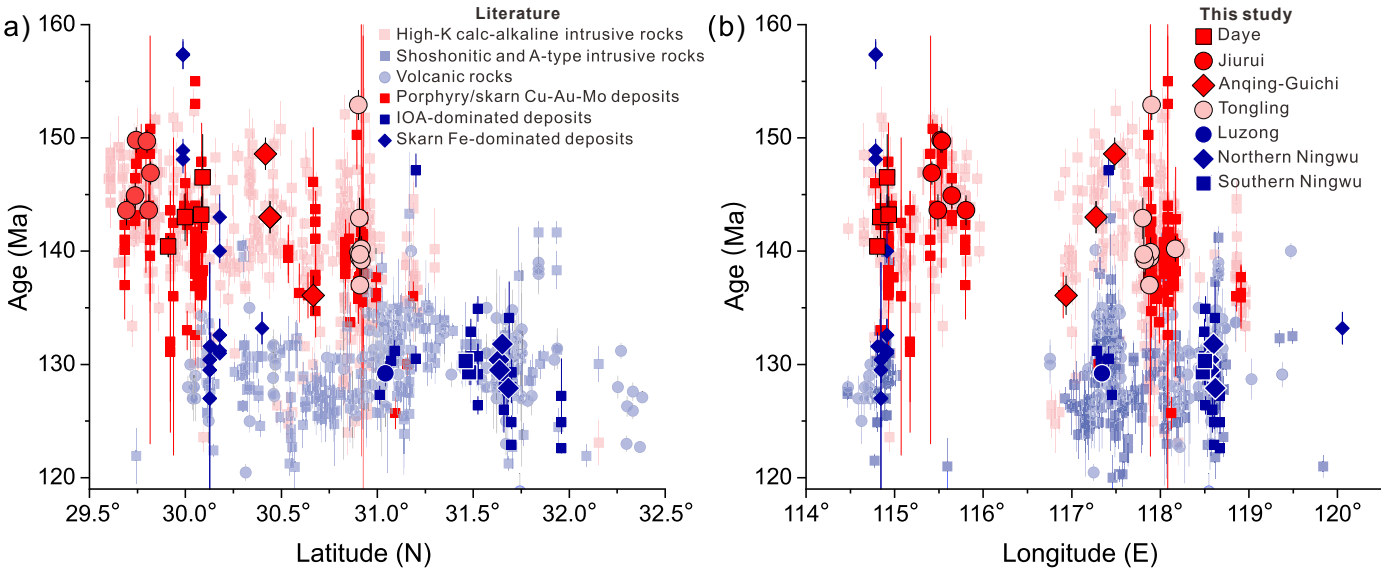

Fig. 3. Plots of previously published age results for igneous rocks and mineralization events versus latitude and longitude in the Middle-Lower Yangtze River metallogenic belt. The zircon U-Pb data in this study are plotted for comparison. See the summary of the previously published age results in Appendix Tables A5 and A6. Error bars represent 2 standard errors. IOA = iron oxide-apatite.

Table 2. Summary of Features for the Studied Representative Ore Deposits in Middle-Lower Yangtze River Metallogenic Belt

Deposit	Ore cluster	Dominated type	Intrusion and the host rocks	Alteration and mineralization	Ore/metal resources	References
Porphyry and skarn Cu ± Au deposits						
Tonglushan	Daye	Skarn Cu-Fe-Au	Quartz monzodiorite/Lower Triassic limestone	Di ± Grt ± Ep ± Phl ± Amp ± Chl ± Serp, Qtz ± Kfs ± Bt, and sodic alteration associated with Ccp ± Bn ± Mt mineralization	Metal resources: 1.08 Mt Cu (@1.78%), 60 Mt Fe (@41%), 70 t Au (@0.38 g/t), and 508 t Ag	Li, J.W., et al. (2014); Zhang et al. (2023)
Tongshankou	Daye	Porphyry ± skarn Cu-Mo	Granodiorite porphyry/Lower Triassic carbonate sequences	(1) Kfs ± Bt ± Qtz and Grt ± Scap ± Ep ± Cal ± Qtz ± Chl ± Serp alteration associated with Ccp ± Py ± Mrc mineralization	Metal resources: 0.5 Mt Cu and 2,000 t Mo	Li et al. (2008); He et al. (2020)
Jiguanzui	Daye	Skarn Au-Cu	Quartz diorite/Lower–Middle Triassic dolomitic marble	Grt ± Py ± Act ± Kfs ± Chl ± Qtz alteration associated with massive, veinlet and disseminated Ccp ± Py ± Mt ± Mol mineralization	Metal resources: 23.3 t Au (@3.93 g/t) and 0.16 Mt Cu (@1.71%)	Zhang et al. (2019); Zhang, Y., et al. (2022)
Baoshan	Jiurui	Porphyry ± skarn Cu	Granodiorite porphyry/Silurian-Ordovician shale, siltstone, dolomite, limestone	Kfs, Qtz-Ser, Cal, and Grt ± Di ± Chl ± Ep ± Act alteration associated with massive, disseminated, and veinlet Ccp ± Py ± Mol mineralization	Not reported	Jia et al. (2015b); Li, Y.M., et al. (2015)
Chengmengshan	Jiurui	Skarn Cu-Au	Granodiorite porphyry, quartz porphyry / Permian to Triassic clastic and carbonate rocks	Grt ± Act ± Di, Kfs and Qtz alteration with minor Ep and Carb alteration associated with disseminated and veinlet sulfide mineralization	Metal resources: 3.07 Mt Cu (@0.75%) and 43.6 t Au (0.24 g/t)	Zhou et al. (2015)
Dongleiwan	Jiurui	Skarn Cu	Granodiorite, granodiorite porphyry/Middle Triassic dolomite and limestone	Grt ± Di ± Qtz ± Calc ± Chl ± Ep alteration associated with Ccp ± Py ± Bn mineralization	Not reported	Jia et al. (2015a)
Jilongshan	Jiurui	Skarn Au-Cu	Granodiorite porphyry/Triassic limestone and dolomites	Grt ± Di ± Act ± Chl ± Qtz ± Ser ± Phl ± Serp ± Ep alteration associated with massive disseminated, veinlet, and breccia Ccp ± Py mineralization.	Metal resources: 44.1 t Au (@3.8 g/t), 0.27 Mt Cu (@1.6%)	Wang, J., et al. (2014); Samake et al. (2018)
Wushan	Jiurui	Porphyry ± skarn Cu	Granodiorite porphyry/ Carboniferous and Permian carbonates	Grt ± Di ± Act ± Ep ± Cal alteration associated with disseminated and veinlet Ccp ± Py ± Mol mineralization	Metal resources: 1.37 Mt Cu (@1.17%)	Xu et al. (2015); Wen et al. (2019)
Tongshan	Guichi	Skarn Cu	Granodiorite porphyry/ Carboniferous–Permian limestone	Grt ± Di ± Serp ± Ep ± Tr ± Ser ± Chl alteration associated with Ccp ± Py ± Bn disseminated and veinlet mineralization	Metal resource: 0.41 Mt Cu (@0.95%) and 10.6 Mt Fe (@39%)	Zhang et al. (2013) and unpublished report
Matou	Guichi	Porphyry ± skarn Cu-Mo	Granodiorite porphyry/Silurian clastic rocks	Kfs ± Qtz ± Ser ± Chl alteration associated disseminated and veinlet Ccp ± Mol mineralization	Metal resource: 12,092 t Cu (@0.29%)	Zhu et al. (2014); Li et al. (2017)
Yueshan	Anqing	Skarn Cu-Au	Diorite/Middle-Lower Triassic marble	Grt ± Di ± Wol ± Ab ± Act ± Tr ±Mus ± Chl ± Ep ± Qtz alteration associated with Ccp ± Po ± Py ± Mol ± Bn mineralization	Metal resource: >0.3 Mt Cu (@2.7%)	Zhou et al. (2007) and unpublished report
Dongguashan	Tongling	Porphyry ± skarn Cu-Au	Quartz monzodiorite (porphyry)/ Permian to Triassic sandstone, limestone and dolomitic limestone	Qtz ± Kfs and Grt ± Di ± Tr ± Ep ± Qtz ± Calc alteration associated with disseminated, veinlet, and massive Ccp ± Py ± Po ± Mt ores	Metal resources: 0.94 Mt Cu (@1.01%) and 22t Au (0.24 g/t)	Zhou et al. (2015); Wang et al. (2015)
Hucun	Tongling	Skarn Cu	Granodiorite/Middle to Lower Triassic carbonate sequences	Grt ± Di ± Ep ± Chl ± Qtz ± Calc alteration associated with Ccp ± Py ± Mol mineralization.	Metal resource: 0.51 Mt Cu (@1.13%)	Zheng and Wen (2017); unpublished report
South Hucun	Tongling	Skarn Cu	Granodiorite porphyry and quartz monzodiorite/Carboniferous to Triassic carbonate sequences.	Grt ± Di ± Ep ± Chl alteration associated with Ccp ± Mo ± Py ± Sph mineralization	Deeper part of Hucun deposit; see metal resource above	Shi et al. (2020)
Jinkouling	Tongling	Skarn Cu	Quartz diorite/Lower Triassic carbonate sequences	Grt ± Di ± Ep ± Qtz ± Cal alteration associated with massive, disseminated, and veinlet Ccp ± Bn mineralization	Metal resource: 55,694 t Cu (@0.97%)	Unpublished report
Shatanjiao	Tongling	Skarn Cu	Granodiorite porphyry/Lower Triassic carbonate sequences	Grt ± Di ± Ep ± Chl ± Act ± Qtz ± Cal alteration associated with disseminated and veinlet Ccp ± Py ± Po mineralization	Metal resource: 46,500 t Cu (@0.73%)	Han and Zhong (2013)
Tongguanshan	Tongling	Skarn Cu	Quartz diorite/Carboniferous and Permian dolomites	Grt ± Di ± Act ± Chl ± Serp ± Qtz ± Cal alteration associated with massive and veinlet Ccp ± Mt ± Po ± Py mineralization	Metal resource: 0.21 Mt Cu (@1.06%)	Fan et al. (2019)

Table 2. (*Cont.*)

Deposit	Ore cluster	Dominated type	Intrusion and the host rocks	Alteration and mineralization	Ore/metal resources	References
Iron oxide-apatite deposits						
Ninghe	Luzong	IOA	Shoshonitic trachyandesitic lava/pyroclastic rocks	Di ± Anh ± Grt ± Ap and later Qtz ± Cal alteration associated with massive and veinlet Mt ± Py mineralization	Ore resource: 183.8 Mt iron ore @ 29.7% Fe and 139.8 Mt FeS ore @ 22.2% S	Wu et al. (2011); Zhang et al. (2014)
Gaocun	Ningwu	IOA	Porphyritic diorite/andesitic sequence	Ab ± Act ± Di ± Ap alteration associated with massive, breccia-hosted, and veinlet Mt mineralization	Ore resource: 200 Mt iron ore @ 22.3% Fe	Ningwu Research Group (1978); Fan et al. (2019)
Heshangqiao	Ningwu	IOA	Porphyritic diorite/andesitic sequence	Ab ± Act ± Di ± Ap alteration associated with massive, breccia-hosted, and veinlet Mt mineralization	Ore resource: 233 Mt iron ore, Fe grade not reported	Duan et al. (2017)
Washan	Ningwu	IOA	Porphyritic diorite/andesitic sequence	Ab ± Act ± Ab ± Ap alteration associated with disseminated, breccia-hosted, and veinlet Mt mineralization	Ore resource: 213.7 Mt iron ore @ 31.8% Fe	Duan et al. (2019)
Hemushan	Ningwu	IOA ± skarn	Porphyritic diorite/Middle-Triassic dolomite interbedded with anhydrite, siltstone, and silty mudstone	Ab ± Phl ± Act ± Di ± Ap alteration associated with massive, disseminated and breccia-hosted Mt mineralization	Ore resource: 83.1 Mt iron ore @ 39.1% Fe	Ningwu Research Group (1978); Zhao et al. (2020); unpublished report
Zhongjiu-Gushan	Ningwu	IOA ± skarn	Porphyritic diorite/Triassic sedimentary sequence	Di ± Ab ± Kao alteration associated with massive, breccia-hosted, veinlet Mt alteration	Ore resource: 184 Mt iron ore @ 35.1%	Ningwu Research Group (1978); Zhao et al. (2020); unpublished report

Abbreviations: Ab = albite, Act = Actinolite, Ap = apatite, Anh = anhydrite, Bn = bornite, Bt = biotite, Cal = calcite, Ccp = chalcopyrite, Chl = chlorite, Di = diopside, Ep = epidote, Grt = garnet, Kao = kaolinite, Kfs = K-feldspar, Mol = molybdenite, Mrc = marcasite, Mt = magnetite, Phl = phlogopite, Po = pyrrhotite, Qtz = quartz, Sph = sphalerite, Ser = sericite, Serp = serpentine, Tr = tremolite, Wol = wollastonite

in these deposits are mainly interpreted to have formed from high-temperature magmatic-hydrothermal saline fluids rather than silicate or Fe oxide melts (Su et al., 2019; Zhao et al., 2020; Zeng et al., 2022).

Petrogenesis of the Ore-Forming Intrusions

The petrogenesis of the igneous rocks in the Middle-Lower Yangtze River metallogenic belt has been studied extensively using lithogeochemical and isotopic methods (cf. Chen et al., 2020; Yang et al., 2021). On primitive mantle-normalized trace element and chondrite-normalized rare earth element (REE) diagrams, both the high-K calc-alkaline and shoshonitic igneous rocks exhibit enrichments in large ion lithophile elements (LILE) and light rare earth elements (LREEs); depletion in Nb, Ta, Ti, P; and a listric-shaped pattern from middle REEs to heavy REEs (Mao et al., 2011; Chen et al., 2020). Such elemental patterns are typical of subduction-related magmas and reflect the fractionation of amphibole, apatite, and Fe-Ti oxides during magma evolution. Most of the high-K calc-alkaline rocks are adakite-like with high La/Yb and Sr/Y ratios and weak to positive Eu anomalies (0.8–1.2), whereas the shoshonitic rocks yielded features of normal arc rocks with lower La/Yb and Sr/Y ratios as well as negative Eu anomalies. Both groups of intrusive rocks yield indistinguishable initial $^{87}Sr/^{86}Sr$ ratios of 0.7050 to 0.7100, suggesting crustal contamination in the source magmas (Mao et al., 2011). The high-K calc-alkaline rocks yielded wider ranges of zircon $\varepsilon_{Hf}(t)$ values (–20 to +2) and whole-rock $\varepsilon_{Nd}(t)$ values (–18 to –2) compared to the shoshonitic rocks, with zircon $\varepsilon_{Hf}(t)$ and whole-rock $\varepsilon_{Nd}(t)$ values clustering at values of –13 to +2 and –10 to –1, respectively (Chen et al., 2020). The most depleted zircon $\varepsilon_{Hf}(t)$ values are from the high-K calc-alkaline granitoids in the Tongling area (Yan et al., 2015; Yang et al., 2021).

Various petrogenetic models have been proposed to explain the origin of the high-K calc-alkaline magmas (Table 1), including remelting of the thickened or delaminated lower crust (Wang et al., 2007; Hou, Z.Q., et al., 2011), interaction of crustal materials with partial melts from the shallow subducted paleo-Pacific slab or from the metasomatized mantle lithosphere at that time (Liu, S.A., et al., 2010; Mao et al., 2011; Yan et al., 2021), or partial melting of mantle lithosphere that was previously metasomatized by slab-derived melts or fluids in the Neoproterozoic (Li et al., 2008; Wang et al., 2016; Chen et al., 2020). In contrast, the shoshonitic rocks associated with IOA deposits were derived mainly from remelting of the lithospheric mantle that was metasomatized by slab-derived fluids (Yuan et al., 2011) either during Mesozoic paleo-Pacific subduction with contamination of crustal materials (Mao et al., 2011; Zhou et al., 2013) or during the Neoproterozoic Jiangnan orogeny (Chen et al., 2020).

Samples and Methods

Sample preparation

Samples were collected from open pits, underground mines, and drill cores from representative porphyry and skarn Cu ± Au and IOA deposits in the Middle-Lower Yangtze River metallogenic belt. One hundred and twenty samples of diorite, quartz diorite, quartz monzonite, and granodiorite with

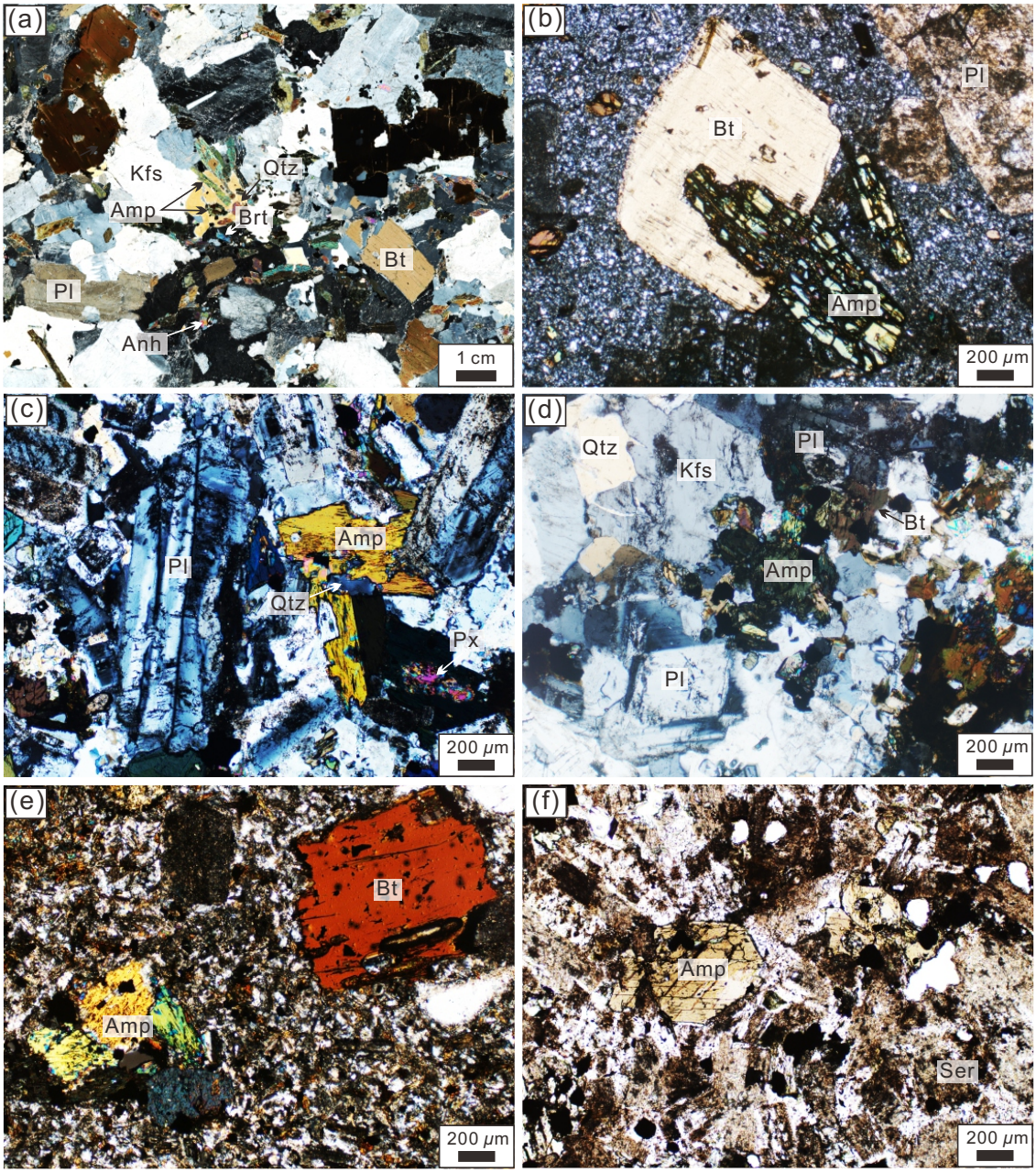

Fig. 4. Photomicrographs of representative least-altered igneous rock samples from the porphyry and skarn Cu ± Au and iron oxide-apatite (IOA) deposits in the Middle-Lower Yangtze River metallogenic belt. (a) Granodiorite porphyry from Tongshankou in the Daye ore district (cross-plane polarized; DYTSK-01). (b) Granodiorite porphyry from Jilongshan in the Jiurui ore district (cross-plane polarized; JRJLS-02). (c) Quartz diorite from Yueshan in the Anqing-Guichi ore district (cross-plane polarized; AQYS-01). (d) Quartz diorite from South Hucun in the Tongling ore district (cross-plane polarized; TLHC-01). (e) Diorite porphyry from the Heshangqiao IOA deposit in the Ningwu ore district (cross-plane polarized; NWHSQ-01). (f) Diorite porphyry from Zhongjiu-Gushan in the Ningwu ore district (plane-polarized; NWZJGS-04). Abbreviations: Amp = amphibole, Anh = anhydrite, Ap = apatite, Brt = barite, Bt = biotite, Kfs = K-feldspar, Pl = plagioclase, Px = pyroxene, Qtz = quartz, Ser = sericite. See Table 3 for sample locations and descriptions.

equigranular or porphyritic textures were collected from the ore-forming plutonic stocks (Fig. 4). Thin sections were prepared for petrographic examination, and most of the collected samples are shown to have been variably altered. Detailed descriptions of these samples are provided in Table 3. Zircon grains from the variably altered samples were separated using conventional magnetic and density methods at the Geological Surveying and Mapping Institute of Hebei Province, China. A total of ~15,000 representative zircon grains were handpicked, mounted on epoxy resins, and polished to expose their internal structures.

To constrain the crystallization conditions and original compositions of the ore-forming magmas, we restricted our analyses to the relatively fresh minerals in the least-altered samples

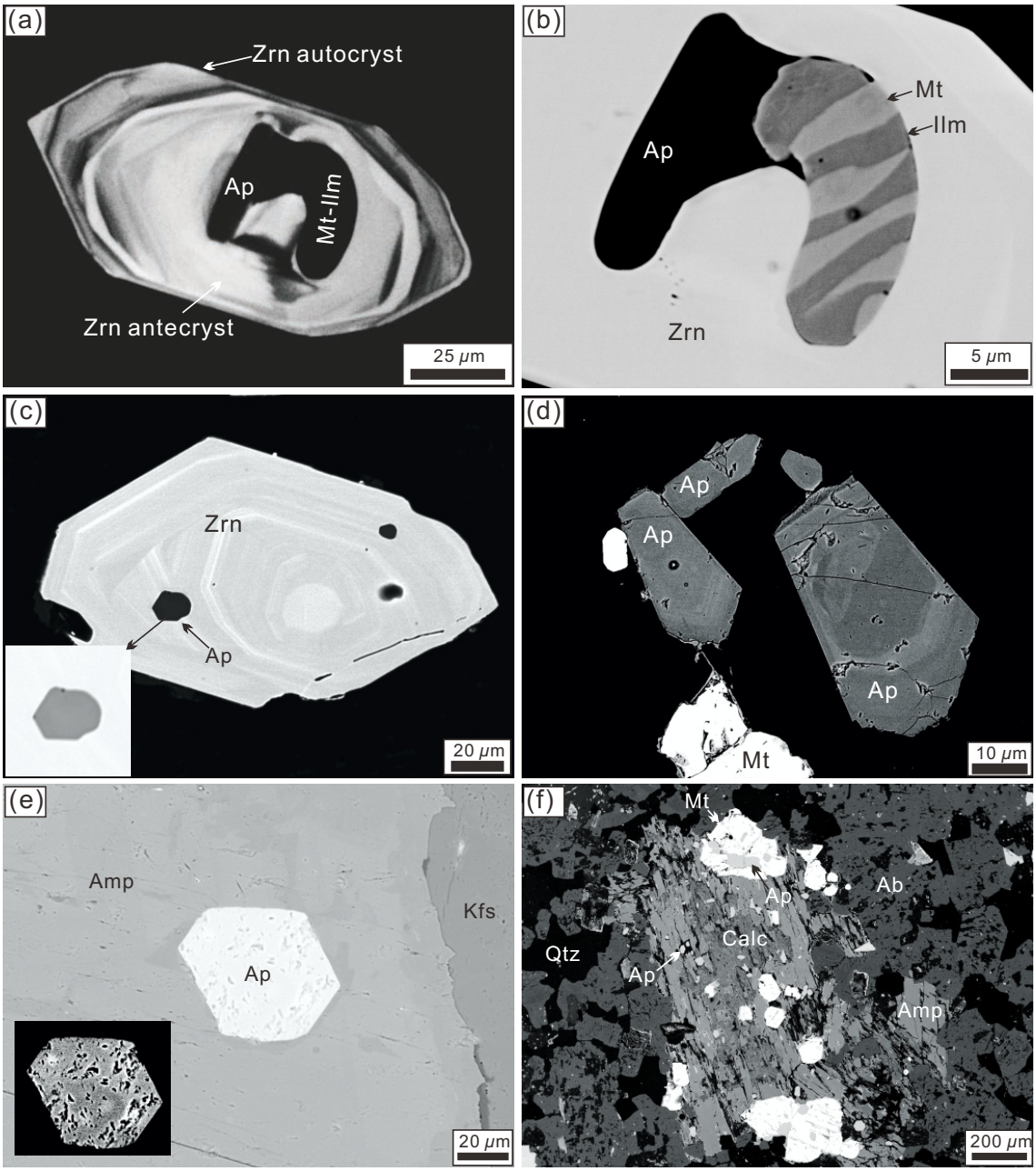

Fig. 5. Photomicrographs of representative magnetite-ilmenite, apatite, and the zircon hosts in the igneous rock samples from the Middle-Lower Yangtze River metallogenic belt. (a, b) Primary magnetite-ilmenite pair in antecrystic zircon core from Jiguanzui in the Daye ore district; cathodoluminescence (CL) and backscattered electron (BSE) images, respectively. (c) Primary apatite inclusion in zircon grain with oscillatory zoning (Washan iron oxide-apatite deposit); BSE. (d) Primary zoned apatite grains in granodiorite from Tongshan in Anqing-Guichi ore district; BSE. (e) Porous, altered apatite inclusion hosted in altered amphibole grain (Yueshan deposit, Anqing-Guichi ore district), BSE. (f) Apatite grains intergrown with quartz, calcite and magnetite (albitized diorite, Heshangqiao, Ningwu ore district). Abbreviations: Ab = albite, Ap = apatite, Calc = calcite, Kfs = K-feldspar, Ilm = ilmenite, Mt = magnetite, Qtz = quartz, Zrn = zircon.

(Fig. 5). Zircon grains and the host mineral inclusions from some altered samples were also analyzed. Amphibole, apatite, biotite, and zircon were analyzed for major and/or trace element abundances using electron probe microanalysis (EPMA) and laser ablation-inductively coupled plasma-mass spectrometry (LA-ICP-MS). Primary amphibole and biotite grains are common in the thin sections for the least-altered high-K calc-alkaline intrusive rock samples but are only rarely observed in the IOA-related dioritic samples (Fig. 4). Magnetite is common as an interstitial phase or as inclusions in other minerals, particularly amphibole. Coexisting magnetite and ilmenite are rarely present as inclusions in zircon grains (e.g., DYJGZ-01, Fig. 5a-b) but seem to form by exsolution from original Fe-Ti oxides. We prioritized analyzing zircon-hosted apatite inclu-

Table 3. Ore-Related Intrusive Samples from the Middle-Lower Yangtze River Metallogenic Belt, China

Sample	District	Deposit	Longitude (E)	Latitude (N)	Elevation (m)	Rock type	Mineralogy (approximated volume percentage)
Porphyry and skarn Cu ± Au deposits							
DYTLS-z01	Daye	Tonglushan	114°56'03"	30°05'01"	40	Quartz diorite	Pl (~60 %), Amp (~20 %), Kfs (~10 %), and Qtz (~10 %); minor Ap, Mt, Ttn, and Zrn
DYTLS-01	Daye	Tonglushan	114°55'59"	30°04'59"	–88	Quartz diorite	Pl (~60 %), Amp (~15 %), Kfs (~10 %), Qtz (~10 %), and Ttn (~2 %); minor Ap, Mt, and Zrn
DYTSK-z01	Daye	Tongshankou	114°50'34"	30°00'27"	37	Granodiorite porphyry	Pl (~35 %), Kfs (~20 %), Qtz (~20 %), Amp (~10 %), Bt (~10 %), and Ttn (~2 %); minor Ap, Zrn, and Anh
DYTSK-01	Daye	Tongshankou	114°50'19"	29°59'54"	–5	Granodiorite porphyry	Pl (~35 %), Kfs (~25 %), Qtz (~20 %), Amp (~10 %), Bt (~5 %), Ttn (~2 %); minor Ap, Zrn, Anh; hydrothermal Py and Ccp (~2 %)
DYHLS-01	Daye	Huanglongshan	114°55'02"	30°05'24"	269	Quartz diorite	Pl (~60 %), Amp (~20 %), Kfs (~10 %), Qtz (~5 %), and Bt (~5 %); minor Ap, Ttn, and Zrn
DYJGZ-01	Daye	Jiguangzui	114°48'25"	29°54'41"	–1,047	Quartz diorite	Altered; phenocrysts: Pl (~30 %); fine-grained groundmass: Pl, Qtz, Kfs; hydrothermal calcite
JRBS-z01	Jiurui	Baoshan	115°31'20"	29°44'39"	148	Granodiorite	Altered; Pl (~60 %), Amp (~20 %), Kfs (~10 %), and Qtz (~10 %); minor Ttn, Ap, Zrn, and Mt; hydrothermal Py
JRCMS-z01	Jiurui	Chengmenshan	115°48'25"	29°41'34"	33	Granodiorite porphyry	Phenocrysts: Pl (~20 %), Bt (~8 %), Qtz (~5 %), and Amp (~2 %); aphanitic groundmass
JRDLW-z01	Jiurui	Dongleiwan	115°32'07"	29°47'59"	121	Granodiorite porphyry	Phenocrysts: Pl (~30 %), Amp (~8 %), Bt (~5 %), and Qtz (~5 %); fine-grained groundmass: Qtz, Pl, and Kfs; minor Ttn, Ap, and Zrn
JRDJS-z01	Jiurui	Dengjiashan	115°29'23"	29°48'34"	146	Granite	Kfs (~40 %), Pl (~30 %), Qtz (~25 %), and Amp (~5 %); minor Ttn, Ap, and Zrn
JRJLS-02	Jiurui	Jilongshan	115°25'08"	29°49'10"	–1	Granodiorite porphyry	Phenocrysts: Pl (~20 %), Amp (~10 %), Bt (~5 %), and Qtz (~5 %); fine-grained groundmass: Pl, Kfs, and Qtz; minor Ap, Zrn, and Mt
JRJLS-03	Jiurui	Jilongshan	115°26'20"	29°48'21"	–150	Granodiorite porphyry	Phenocrysts: Pl (~15 %), Amp (~15 %), Bt (~5 %), and Qtz (~5 %); aphanitic groundmass (~60 %); minor Ap, Zrn, and Mt
JRWS-z01	Jiurui	Wushan	115°38'46"	29°44'15"	58	Granodiorite porphyry	Phenocrysts: Pl (~30 %) and Bt (~5 %); fine-grained groundmass: Pl, Kfs, and Qtz
GCTS-03	Guichi	Tongshan	117°16'23"	30°26'26"	–195	Granodiorite	Pl (~35 %), Kfs (~25 %), Qtz (~15 %), Amp (~10 %), Bt (~8 %), and Mt (~2 %); minor Ap and Zrn
GCMT-01	Guichi	Matou	117°29'02"	30°25'02"	–243	Granodiorite porphyry	Phenocrysts: Pl (~35 %), Bt (~10 %), Qtz (~5 %), Amp (~5 %), and Kfs (~5 %); groundmass: Qtz (~20 %), Pl (~10 %), Bt (~5 %), and Mt (~2 %); minor Ap, Zrn, and Ttn
AQYS-03	Anqing	Yueshan	116°56'14"	30°39'57"	–37	Quartz diorite	Pl (~55 %), Qtz (~10 %), Kfs (~15 %), Amp (~20 %), Ttn (~2 %), and Mt (~2 %); minor Ap and Zrn
TLDGS-01	Tongling	Dongguashan	117°52'41"	30°54'35"	–109	Quartz diorite	Pl (~45 %), Kfs (~20 %), Qtz (~20 %), and Amp (~10 %); minor Ttn, Zrn, Ap, and Mt
TLDGS-z01	Tongling	Dongguanshan (Qingshanjiao)	117°52'53"	30°54'35"	19	Quartz monzodiorite	Altered; Pl (~35 %), Kfs (~30 %), Qtz (~15 %), Amp (~10 %), and Mt (~5 %); hydrothermal Py and Ccp
TLHC-z01	Tongling	Hucun	117°53'02"	30°54'24"	20	Quartz diorite	Pl (~60 %), Px (~30 %), and Qtz (~10 %); minor Ttn, Mt, Ap, and Zrn
TLHC-01	Tongling	South Hucun	117°53'28"	30°54'10"	–1,650	Granodiorite	Pl (~50 %), Kfs (~20 %), Qtz (~10 %), Bt (~10 %), and Amp (~5 %); minor Ttn, Ap, Zrn, and Mt; interstitial Anh
TLJGS-z01	Tongling	Jiguangshan	117°54'07"	30°54'06"	21	Quartz diorite	Pl (~70 %), Kfs (~5 %), Amp (~10 %), Qtz (~5 %), and Mt (~2 %); minor Ttn, Ap, and Zrn
TLJKL-z01	Tongling	Jinkouling	117°48'09"	30°54'26"	12	Quartz diorite	Pl (~60 %), Amp (~15 %), Kfs (~10 %), Qtz (~10 %), and Bt (~2 %); minor Ttn, Ap, and Zrn
TLSTJ-z01	Tongling	Shatanjiao	118°10'04"	30°55'05"	46	Granodiorite	Pl (~60 %), Qtz (~20 %), Bt (~10 %), and Kfs (~10 %); minor Ap, Zrn, and Mt
TLTEB-z01	Tongling	Tianebaodan	117°49'40"	30°55'05"	15	Quart diorite	Pl (~60 %), Amp (~15 %), Qtz (~10 %), Mt (~8 %), and Kfs (~5 %); minor Ap, Zrn
TLTGS-02	Tongling	Tongguanshan	117°48'50"	30°54'29"	116	Quartz diorite	Pl (~50 %), Px (~35 %), Kfs (~10 %), and Ttn (~2 %); minor Qtz, Ttn, Ap, Zrn
TLTGS-z01	Tongling	Tongguanshan	117°48'45"	30°54'32"	13	Quartz diorite	Pl (~60 %), Amp (~20 %), Kfs (~5 %), and Qtz (~5 %); minor Mt, Ttn, Ap, Zrn

Table 3. (*Cont.*)

Sample	District	Deposit	Longitude (E)	Latitude (N)	Elevation (m)	Rock type	Mineralogy (approximated volume percentage)
Iron oxide-apatite deposits							
LZNH-06	Luzong	Nihe	117°20′28″	31°02′30″	–986	Diorite	Highly altered; primary minerals cannot be identified, containing Di (~70 %) and Anh (~30 %)
NWGC-02	Ningwu	Gaocun	118°37′17″	31°40′59″	11	Diorite	Highly altered with Ab, Act, Ser, and Mt
NWHSQ-01	Ningwu	Heshangqiao	118°33′05″	31°37′59″	–63	Diorite porphyry	Phenocrysts: Pl (~25 %), Bt (~5 %), and Amp (~5 %); fine-grained groundmass: Pl, Bt, minor Qtz; minor Mt, Ap, Zrn
NWHSQ-04	Ningwu	Heshangqiao	118°33′05″	31°38′10″	–15	Diorite porphyry	Phenocrysts: Pl (~30 %) and Amp (~10 %); fine-grained groundmass: Pl, Qtz; minor Mt, Ttn, Ap, Zrn
NWWS-02	Ningwu	Washan	118°35′59″	31°39′04″	–52	Diorite porphyry	Phenocrysts: Pl (~50 %) and Act (~15 %); fine-grained groundmass: Pl, Qtz, Act; minor Mt, Ttn, Ap, Zrn
NWHMS-01	Ningwu	Hemushan	118°28′49″	31°28′44″	–668	Diorite	Altered; Pl (~90 %) and Act (~10 %); interstitial Anh; minor Mt, Ttn, Ap, Zrn
NWZJGS-01	Ningwu	Zhongjiu-Gushan	118°30′18″	31°27′40″	–1,449	Diorite	Altered; Pl (~70 %), Amp (~20 %), and Mt (~5 %); minor Qtz, Mt, Ttn, Ap, Zrn, Amp

Abbreviations: Ab = albite, Act = actinolite, Amp = amphibole, Anh = anhydrite, Ap = apatite, Bt = biotite, Di = diopside, Ilm = ilmenite, Kfs = K-feldspar, Mt = magnetite, Pl = plagioclase, Px = pyroxene, Ser = sericite, Ttn = titanite, Zrn = zircon

sions (Fig. 5c) that preserve primary chemical zoning (Fig. 5d), or compositionally homogeneous apatite grains hosted in mineral phases such as amphibole and biotite. Porous apatite grains or those intergrown with hydrothermal minerals (e.g., sample NWHSQ-04) are interpreted to have been altered (Fig. 5e) or crystallized from magmatic fluids exsolved from silicate melt (Fig. 5f). All studied zircon grains exhibit oscillatory or sector zonings, as revealed by cathodoluminescence (CL) imaging (Fig. 5a, c; App. Figs. A1 and A2).

LA-ICP-MS zircon U-Pb and trace element analyses

Zircon grains were analyzed for U-Pb isotope and trace element abundances using LA-ICP-MS at the Collaborative Innovation Center for Exploration of Strategic Mineral Resources, China University of Geosciences (Wuhan). A 193-nm NWR HE excimer laser coupled with an Agilent 7900 ICP-MS was used to ablate and analyze the zircon grains. The parameters for the laser were a fluence of 3.5 J/cm^2, a repetition rate of 8 Hz, and a spot size of 32 µm. Thirty seconds of background were acquired followed by each analysis of 40 s. Primary and secondary reference materials for the zircon U-Pb isotope and trace element analyses were analyzed regularly during the analytical sessions.

Correction of laser-induced element fractionation, instrumental drift, and downhole fractionation was performed with ICPMSDataCal software (Liu, Y., et al., 2010). The U-Pb isotope ratios were normalized to the primary zircon reference material 91500. The secondary reference materials SA-01 or Qinghu-01 were analyzed to monitor the accuracy and reproducibility of the unknown isotopic analyses. The trace element data were normalized using an internal standard scheme to the synthetic glass NIST610 with an assumption of the stoichiometric concentration of Si in zircon as 15.32 wt %. The synthetic glass NIST612 and zircon 91500 were used to monitor the accuracy of the unknown trace element analyses. The isotopic and trace element data for the secondary reference materials are consistent with the reported standard values (App. Table A1). Concordia or intercept ages for the samples were calculated using Isoplot v. 4.15 (Ludwig, 2012), in which the uncertainties of the uranium decay constants are considered. The values of the mean square of weighted deviates (MSWD) for the studied samples are calculated to measure the ratio of the scatter of the data points to the predicted scatter due to the analytical uncertainty (Wendt and Carl, 1991). To minimize the effects of hydrothermal alteration and contamination of subsurface mineral/melt inclusions on T-f_{O_2} results, the zircon trace element data were screened using criteria as follows: (1) La content < 1 ppm, (2) LREE index (Dy/Nd + Dy/Sm) > 10 (Bell et al., 2016); (3) Ti < 50 ppm (Lu, 2016).

Electron probe microanalysis (EPMA)

Major and trace element abundances of amphibole, biotite, and apatite were acquired using a JOEL JXA-iHP200F field emission EPMA at the Institute of Mineral Resources, China Academy of Geological Sciences. The analytical parameters varied for the different analyzed minerals. Amphibole and biotite were analyzed for twelve elements (i.e., Si, Ti, Al, Cr, Fe, Mn, Mg, Can, Na, K, F, and Cl) at the same conditions: 15-kV accelerating voltage, 20-nA beam current, and 5-µm spot beam size.

Apatite grains were analyzed for fourteen elements (i.e., P, Ca, Al, Si, Mn, Fe, Sr, Y, Na, K, F, Cl, S, and Zr) using the following conditions: 15-kV accelerating voltage, 10-nA beam current, and beam sizes from 2 to 5 µm depending on the size of the analyzed grain. Meng et al. (2021a) used these analytical conditions for apatite and reported that (1) the measured S and Cl contents of apatite are more reliable than F content when using a 2-µm beam, and (2) damage of apatite using a beam size of 5 µm can be minimized, particularly for apatite grains with the c-axis perpendicular to the electron beam (Meng et al., 2021a). In this study, we only report the F content of apatite for analyses that used a beam size of 5 µm or for grains where the c-axis was perpendicular to the 2-µm beam.

X-ray lines, crystals, internal standards, and counting times for peak and background measurements are provided in the notes of Appendix Tables A2 through A4. We excluded all analyses of zircon-hosted apatite grains with ZrO_2 concentration of >1 wt %, as these are interpreted to reflect contamination of the inclusion by the host.

Methods of T-P- f_{O_2} estimation

The crystallization temperatures of apatite, zircon, and amphibole were estimated using the methods in Piccoli and Candela (1994), Loucks et al. (2020), and Ridolfi (2021), respectively. For estimating apatite saturation temperature (AST), we used previously compiled lithogeochemical data for the studied intrusive rocks (Chen et al., 2020) and assumed the whole-rock SiO_2 and P_2O_5 abundances approximate those in the silicate melts at the time of apatite crystallization. A revised Ti-in-zircon thermometer by Loucks et al. (2020) was used to constrain zircon crystallization temperatures ($T_{Ti\text{-}Zr}$), considering it includes the effect of pressure on the calibration of Ferry and Watson (2007). The activities of SiO_2 and TiO_2 were assumed to be 1 and 0.6, respectively, based on the presence of primary quartz and titanite as well as zircon-hosted ilmenite in the samples (Tables 3, 4; Dilles et al., 2015; Schiller and Finger, 2019). The crystallization pressure of the amphibole grains was estimated using the amphibole barometer of Mutch et al. (2016).

Values of f_{O_2} for the ore-forming magmas were estimated from the compositions of zircon and amphibole using the oxybarometers of Loucks et al. (2020) and Ridolfi (2021). We attempted to use the zircon oxybarometers calibrated by Smythe and Brenan (2016) and Loucks et al. (2020). The method of Smythe and Brenan (2016) requires quantitative determination of trace element abundances in zircon and the zircon-equilibrated melt composition in addition to water content and the activities of SiO_2 and TiO_2 (i.e., $a$$SiO_2$ and $a$$TiO_2$). This method is sensitive to water content, where a variation of 1 wt % H_2O in the melt can lead to a deviation of ~0.5 log units of f_{O_2}. Considering that we currently lack a robust method for accurately estimating the absolute water content at the time of zircon crystallization, the empirical zircon oxybarometer of Loucks et al. (2020) that only involves the measured concentrations of Ti and Ce and the age-corrected initial U concentration of zircon was used. The zircon Ce-Ti-U_i oxybarometer was calibrated by Loucks et al. (2020) using f_{O_2} values determined from coeval magnetite-ilmenite pairs and amphibole, melt Fe^{3+}/Fe^{2+} ratios, and experimental run products at controlled f_{O_2}. Loucks et al.'s (2020) method is applicable to igneous rocks with a broad compositional range (i.e., calc-alkaline, tholeiitic, adakitic, shoshonitic, metaluminous to mildly peraluminous, and mildly peralkaline) with f_{O_2} values of ΔFMQ –4.9 to ΔFMQ +2.9. The estimated f_{O_2} value yields a standard error of ~ ±0.6 log unit.

The amphibole oxybarometer was calibrated using experimental data of amphibole in equilibrium with the calc-alkaline and alkaline silicate melts under various f_{O_2} conditions (Ridolfi et al., 2010; Ridolfi and Renzulli, 2012; Ridolfi, 2021). We used the most recently updated amphibole oxybarometer that was calibrated by filtering out poor-quality experimental data (Ridolfi, 2021). The oxybarometer is P-T-independent and is suitable for Mg-rich calcic amphibole in calc-alkaline and alkaline melts across a wide P-T range (up to 2,200 MPa and 1,130°C). The spreadsheet Amp-TB2 in Ridolfi (2021) was used to assess the reliability and suitability of the amphibole EPMA analyses for the oxybarometer. We excluded analyses that were outside the compositional range for calibrating the amphibole oxybarometer. The standard error for the amphibole oxybarometer is ±0.3 log units.

Methods in estimating melt volatile concentrations

We tried to use multiple mineral-based methods to estimate concentrations of H_2O, S, and Cl in the silicate melts from which the ore-forming magmatic-hydrothermal fluids exsolved. The H_2O content was approximated using the amphibole hygrometer of Ridolfi (2021). However, because the coefficient of determination for the linear relationship between experimental and calculated H_2O contents using the amphibole hygrometer is low (R^2 = 0.645; Ridolfi, 2021), we suggest that the H_2O results can only be regarded as semi-quantitative. The S concentration in the melt was estimated using a model for the partition coefficient of S between apatite and melt ($D_S^{ap/m}$; Meng et al., 2021a) based on experimental studies that demonstrated the S concentration in apatite is controlled by the melt S content, f_{O_2}, and temperature (Parat and Holtz, 2004; Konecke et al., 2019). The melt Cl/H_2O ratio was estimated using methods as follows: (1) an exchange partitioning model (Li and Hermann, 2017) established based on experimental results of felsic silicate melts by Webster et al. (2009), (2) a thermodynamic exchange partitioning model that considers the nonideality in apatite solid solution (Li and Costa, 2020), (3) an exchange coefficient model for partitioning of Cl-OH between amphibole and melt as a function of amphibole composition (Giesting and Filiberto, 2014), and (4) an empirical exchange coefficient model for Cl-F-OH partitioning between biotite and silicate melt as functions of the compositions of the biotite and the equilibrated melt (Zhang, C., et al., 2022). For method (4), we assumed the whole-rock compositions summarized by Chen et al. (2020) represent the melt composition.

Results

Zircon U-Pb dating

The absolute timing of the igneous rocks has been well constrained mainly using zircon U-Pb dating by a number of authors (Fig. 3; App. Table A5). We supplement the cathodoluminescence (CL) images and U-Pb dates for the zircon samples in order to distinguish the antecrystic, autocrystic,

and xenocrystic zircon grains. A total of 429 isotopic analyses were performed. Most analyses yielded Th/U ratios of >0.3 (App. Table A1), and the analyzed grains typically exhibit oscillatory and sector zonings consistent with a magmatic origin (App. Figs. A1 and A2). The U-Pb isotope data for the xenocrystic and antecrystic cores were distinguished based on their morphologies (Corfu et al., 2003). Zircon xenocrysts typically yielded older $^{206}Pb/^{238}U$ dates compared to the concordia or intercept U-Pb ages, whereas the antecrystic zircon cores yielded indistinguishable $^{206}Pb/^{238}U$ dates (App. Table A1) but contrasting chemical zoning in CL responses that contrast the rims (Fig. 5a).

Geochronological data are summarized in Table 4 and illustrated in Appendix Figures A3 and A4. Concordia, or intercept U-Pb ages, were calculated to define the crystallization ages of the dated zircon grains and the host intrusive rocks. Consistent with previous studies (Figs. 2b, 3; App. Tables A5–A6), the geochronological results suggest that the magmas related to porphyry and skarn Cu deposits and IOA deposits in the Middle-Lower Yangtze River metallogenic belt intruded the upper crust at 150 to 135 and ~130 Ma, respectively (Table 4). The porphyry- and skarn-related igneous rocks contain abundant zircon xenocrysts that yielded U-Pb dates of 3443 to 739 Ma (n = 32), which is consistent with the age spectrum of the zircon xenocrysts entrapped by lamprophyres in Middle-Lower Yangtze River metallogenic belt (Zhang, S., et al., 2021). Nineteen Jurassic xenocrystic zircon grains were identified in porphyry- and skarn-related intrusive rocks, whereas only one Triassic zircon grain was identified in the IOA-related samples (App. Table A1).

T-P conditions

The estimated crystallization temperatures of various mineral phases and the estimated crystallization pressures of amphibole for representative samples are summarized in Table 5 and illustrated in Figures 6a, b, 7a, 8, 9a, and 10. The zircon and amphibole record comparable crystallization temperatures of 700° to 950°C (Figs. 6a, b, 8a) and 650° to 900°C (Figs. 6a, b, 8b), respectively. Assuming $a\mathrm{TiO_2}$ = 0.6 and $a\mathrm{SiO_2}$ = 1.0, the $T_{Ti\text{-}Zr}$ values for dioritic rocks associated with IOA deposits are greater than $T_{Ti\text{-}Zr}$ values for granodioritic to quartz dioritic rocks from porphyry and skarn deposits (890° ± 50° vs. 810° ± 50°C; 1σ; Table 5; Fig. 6a). No time-space variations in $T_{Ti\text{-}Zr}$ values are observed for the igneous rocks associated with porphyry and skarn Cu ± Au deposits across the four porphyry and skarn ore districts (Figs. 6a, b, 7). In contrast, the crystallization temperatures of amphibole in the intrusive rocks associated with the porphyry and skarn and IOA deposits are comparable at 770° ± 40°C (1σ) and 750° ± 50°C (1σ), respectively (Table 5).

The amphibole grains are classified as Mg-hornblende except for one sample that contains Mg-hastingsite and Tschemakitic pargasite (App. Table A2). The crystallization pressures for amphibole from the porphyry- and skarn-related intrusive rocks range from 527 ± 60 MPa (1σ) to 118 ± 30 MPa (1σ), whereas amphibole in the IOA-related diorite samples crystallized at pressures of 189 ± 72 to 85 ± 16 MPa (1σ; Table 5), corresponding to crystallization paleo-depths of 5 to 20 and 3 to 7 km, respectively. Amphibole barometry indicates that amphibole in the porphyry- and skarn-related intrusive rocks crystallized along a steeper P-T trajectory compared to amphibole from the magmas associated with IOA mineralization (Fig. 10a).

Magmatic f_{O_2} estimates

The magmatic f_{O_2} estimates for representative intrusive samples from porphyry and skarn Cu and IOA deposits are reported in Table 5 and illustrated in Figures 6c, d, 7b, 8, and 10b. Geochemical data for zircon from Wang et al. (2013), Wang et al. (2015), Wen et al. (2020), and Zhang, J., et al. (2021) were included in the reported f_{O_2} values.

Zircon: Zircon grains from the porphyry- and skarn-related intrusive rocks yielded average magmatic f_{O_2} values of ΔFMQ + 0.5 ± 0.6 (1σ) to + 2.2 ± 0.3 (1σ) at temperatures of 930° to 740°C (Figs. 6c, d, 7b, 8a, b). There are no time-space variations in ΔFMQ values for the igneous rocks associated with porphyry and skarn Cu ± Au deposits across the four ore districts (Figs. 6c, d, 7b). With the exception of one sample, the average magmatic f_{O_2} values for samples from the Edong, Jiurui, and Anqing-Guichi ore districts increase from ~ΔFMQ +0.7 at 930°C to ~ΔFMQ +2.5 at ~800°C, and then decline to ~ΔFMQ +1 at ~740°C (Fig. 8a; Table 5). A strong negative correlation between ΔFMQ values and $T_{Ti\text{-}Zr}$ is observed for samples from the Tongling district, culminating in an ΔFMQ value of +2.2 ± 0.3 at 775° ± 37°C (1σ; Fig. 8a). The negative correlation of estimated f_{O_2} with $T_{Ti\text{-}Zr}$ was also detected for single samples from the other ore districts studied. Five antecrystic zircon cores from Jiguanzui in the Daye district yielded a ΔFMQ value of +0.7 ± 0.2 (1σ) at 933° ± 21°C (1σ), whereas 10 analyses of autocrystic zircon grains from the same sample yielded higher average ΔFMQ value of +1.9 ± 0.3 (1σ) at lower $T_{Ti\text{-}Zr}$ of 788° ± 28°C (1σ; Table 5). Similarly, three analyses of the antecrystic zircon cores from Tongshan in the Anqing-Guichi district yielded a ΔFMQ value of +0.7 ± 0.3 (1σ) at 896° ± 10°C (1σ) compared to autocrystic zircon grains from the same sample that yielded a ΔFMQ value of +1.6 ± 0.4 (1σ) at 817° ± 29°C (1σ; Table 5).

The estimated magmatic f_{O_2} values of the IOA-related magmas are highly variable (Table 5) and are on average lower than the porphyry- and skarn-related magmas (Figs. 6b, 7b). The IOA-related samples have been divided into three groups (Figs. 6b, 7b, 8b): (1) a sample from Nihe in the Luzong ore district yielded ΔFMQ –1.4 ± 0.2 (1σ); (2) four samples from the northern Ningwu ore district yielded increasing f_{O_2} values (from ΔFMQ –0.8 ± 0.4 to ΔFMQ +0.6 ± 0.3) with decreasing temperatures; (3) two samples from the southern Ningwu ore district yielded greater FMQ values of 1.2 ± 0.7 (1σ) and 2.1 ± 0.4 (1σ; Table 5).

Thirty-two Archean-Proterozoic zircon xenocrysts from the porphyry- and skarn-related intrusive rocks yielded an average magmatic f_{O_2} value of ~ΔFMQ +0.1 ± 1.6 (1σ, n = 32; Fig. 8c; App. Table A1). Most of the zircon grains yielded U_i/Nb ratios of ≥40 (U_i represents the age-corrected initial U concentration in zircon calculated following the method in Loucks et al., 2020; Fig. 8c). In comparison, fourteen xenocrystic zircon grains of Jurassic ages yielded a higher average f_{O_2} value of ΔFMQ +1.4 ± 0.5 (1σ, n = 14; Fig. 8c; App. Table A1). The Triassic xenocrystic zircon grain identified in one sample from the Heshangqiao IOA deposit yielded an f_{O_2} value of ΔFMQ +0.4 ± 0.4 (2SE).

Table 4. Zircon U-Pb Ages and Mineral Inclusions and the Analyzed Primary Mineral for Representative Ore-Related Intrusive Samples from the Middle-Lower Yangtze River Metallogenic Belt, China

Sample	Zircon-hosted inclusion	Zrn U-Pb age (Ma, 2σ)	MSWD	n	Description of zircon U-Pb isotope data	Primary mineral			
						Zrn	Amp	Ap	Bt
Porphyry and skarn Cu ± Au deposits									
DYTLS-z01	n.a.	143.2 ± 1.6	0.05	16	All analyses are concordant or near-concordant; no xenocrystic zircon grains have been identified	√			
DYTLS-01	n.a.	~143 [1]			n.a.		√	√	
DYTSK-z01	n.a.	143.0 ± 2.1	0.71	12	Concordia intercepted age; another concordia intercept age of 154.7 ± 7.8 Ma (MSWD = 0.023, n = 3) was obtained for 3 other analyses	√			
DYTSK-01	Ap, Qtz	~143 [1]			n.a.		√	√	√
DYHLS-01	n.a.	146.5 ± 3.8	0.37	7	Concordia intercept age; one concordant analysis yielding older $^{206}Pb/^{238}U$ date was excluded	√	√	√	√
DYJGZ-01	Ap, Ab, Kfs, Pl, Px, Qtz, Mt-Ilm	140.4 ± 0.9	0.59	15	Concordia age; one Mesoproterozoic zircon core has been identified	√		√	
JRBS-z01	n.a.	149.8 ± 1.1	0.18	13	Concordia age; two concordant analyses yielding slightly older $^{206}Pb/^{238}U$ dates were excluded; two Jurassic zircon cores have been identified (167–173 Ma)	√			
JRCMS-z01	n.a.	143.6 ± 1.3	1.7	11	Concordia intercept age; two Neoproterozoic (623–774 Ma) and two Jurassic (164–168 Ma) zircon cores have been identified	√			
JRDLW-z01	n.a.	149.7 ± 1.0	1.7	14	Concordia age	√			
JRDJS-z01	n.a.	143.6 ± 1.4	0.47	13	Concordia age	√			
JRJLS-02	n.a.	~147 [1]			n.a.		√	√	√
JRJLS-03	n.a.	146.9 ± 1.0	1.11	12	Concordia intercept age; two concordant analyses with slightly older $^{206}Pb/^{238}U$ dates were excluded; one Mesoproterozoic (~1,510 Ma) zircon core is identified	√			
JRWS-z01	n.a.	144.9 ± 1.1	0.01	12	Concordia age; one Neoproterozoic (~900 Ma) zircon core is identified	√			
GCTS-03	Ap, Kfs, Ttn	143.0 ± 1.4	1.0	14	Concordia intercept age; three analyses are highly discordant; xenocrystic zircon cores of Neoarchean (~2,595–2,656 Ma), Paleoproterozoic (~1,940 Ma), Neoproterozoic (~838 Ma), and Jurassic (~171 Ma) ages have been identified	√	√	√	
GCMT-01	Ap, Bt, Kfs, Qtz, Mt-Ilm	148.6 ± 1.4	0.04	8	Concordia age	√	√	√	√
AQYS-03	Amp, Bt, Kfs, Mt, Qtz	136.1 ± 1.7	1.4	15	Concordia intercept age	√	√	√	
TLDGS-01	Ap, Kfs	~137 [2]			n.a.	√	√	√	
TLQSJ-z01	n.a.	141.1 ± 1.3	0.19	10	Concordia age; another concordia age of 154.1± 2.6 Ma (MSWD = 0.51, n = 4) is obtained for the other 4 discordant analyses; one Mesoproterozoic (~1,439 Ma), 1 Neoproterozoic (~920 Ma), and 4 Jurassic (~152–157 Ma) zircon grains have been identified	√			
TLHC-z01	n.a.	139.4 ± 0.9	0.53	13	Concordia age; one Paleoproterozoic (~1,772 Ma) and one Neoproterozoic (~776 Ma) zircon cores have been identified	√			
TLHC-01	Amp, Ap, Bt, Mt, Ilm	139.9 ± 1.3	0.02	7	Concordia age	√	√	√	
TLJGS-z01	n.a.	152.9 ± 1.3	0.02	12	Concordia intercept age; one discordant analysis was excluded; one Paleoproterozoic (~2,117 Ma) zircon core has been identified	√			
TLJKL-z01	n.a.	135.3 ± 1.5	1.05	6	Concordia age; with another concordia age of 142.9 ± 1.8 Ma (MSWD = 0.04, n = 6) for the other 6 concordant analyses; one discordant analysis was excluded; one Neoarchean (~2,692 Ma), 5 Paleoproterozoic (~2,406–1,966 Ma), 3 Neoproterozoic (~694–849 Ma) zircon cores have been identified	√			
TLSTJ-z01	n.a.	140.2 ± 1.1	4.7	14	Concordia age; with 6 highly discordant analyses and 2 older concordant analyses yielding older $^{206}Pb/^{238}U$ dates were excluded	√			
TLTEB-z01	n.a.	139.2 ± 1.3	0.24	11	Concordia intercept age; with one concordant analysis yielding older $^{206}Pb/^{238}U$ date and one younger zircon grains (possibly reflect Pb loss) excluded; one Neoarchean (~2,531 Ma), 3 Paleoproterozoic (~1,636–1,920 Ma), 2 Neoproterozoic, and 1 Jurassic zircon cores have been identified	√			
TLTGS-02	Ap, Bt, Ilm, Qtz	~140 [1]			n.a.			√	
TLTGS-z01	n.a.	139.7 ± 2.6	0.49	10	Concordia intercept age; one Paleoproterozoic (~2,269 Ma), 1 Triassic, and two Jurassic zircon cores have been identified	√			

Table 4. (*Cont.*)

Sample	Zircon-hosted inclusion	Zrn U-Pb age (Ma, 2σ)	MSWD	n	Description of zircon U-Pb isotope data	Primary mineral			
						Zrn	Amp	Ap	Bt
Iron oxide-apatite deposits									
LZNH-06	Kfs, Qtz, Mt	129.2 ± 1.1	0.27	15	Concordia intercept age; with one analysis yielding older $^{206}Pb/^{238}U$ date excluded	√			
NWGC-02	Ab, Mt	127.9 ± 1.2	0.37	10	Concordia intercept age; with one concordant analysis yielding older $^{206}Pb/^{238}U$ date and one discordant analysis (possibly reflecting Pb loss) excluded	√			
NWHSQ-01	Ap, Bt, Ccp, Px, Py, Po, Qtz, Ttn, and Mt-Ilm	130.4 ± 1.0	0.01	15	Concordia age; one Permian–Triassic (~252 Ma) zircon grain has been identified	√	√	√	√
NWHSQ-04	Ap, Qtz	129.5 ± 0.9	0.54	15	Concordia intercept age; one analysis with younger $^{206}Pb/^{238}U$ date (possibly reflecting Pb loss) excluded	√	√	√	
NWWS-02	Ab, Kfs, Ilm, Mnt, Mt, Px, Qtz	131.8 ± 0.9	0.68	16	Concordia intercept age	√		√	
NWHMS-01	Ap, Px, Pl	129.3 ± 1.1	0.48	7	Concordia intercept age	√		√	
NWZJGS-01	Ab, Ap, Bt, Kfs, and Qtz	130.3 ± 0.9	1.2	15	Concordia age; one analysis with slightly older $^{206}Pb/^{238}U$ date was excluded	√	√	√	

Note: The superscripts against the zircon U-Pb ages indicate the approximate values from (1) this study or (2) Zhang, J., et al. (2021)
Abbreviations: Ab = albite, Amp = amphibole, Ap = apatite, Bt = biotite, Ilm = ilmenite, Kfs = K-feldspar, Mt = magnetite, Mnt = monazite, Pl = plagioclase, Px = pyroxene, Qtz = quartz, Ttn = titanite, Zrn = zircon; MSWD = mean square of weighted deviates

All the analyzed zircon grains from the studied samples yielded negative Eu anomalies (Figs. 6e, f, 7c, 9). The porphyry- and skarn-related intrusive rocks typically yielded higher zircon Eu/Eu* ratios of 0.62 ± 0.08 (ranging from 0.43 ± 0.04 to 0.77 ± 0.08; 1σ) compared to those for IOA deposits (0.43 ± 0.09 on average; ranging from 0.33 ± 0.04 to 0.53 ± 0.09; 1σ). No time-space variations in zircon Eu/Eu* values are observed for the igneous rocks associated with porphyry and skarn Cu ± Au deposits across the four ore districts (Figs. 6e, f, 7c). A positive correlation between the Eu/Eu* and ΔFMQ values has not been observed (Fig. 9b), suggesting the magmatic f_{O_2} may not be the main factor affecting the zircon Eu/Eu* anomalies reported here.

Amphibole: The average magmatic f_{O_2} value estimated from amphibole compositions for the porphyry- and skarn-related intrusive rock samples is ΔFMQ +1.6 ± 0.4 (1σ), which is lower than that for IOA deposits (ΔFMQ +2.4 ± 0.3, 1σ; Table 5). The magmatic f_{O_2} values for the samples from porphyry- and skarn-related deposits decrease from ΔFMQ ~2.3 ± 0.4 at 838° ± 42°C to a scattered range of ΔFMQ +1.0 to 1.5 at lower temperatures (Fig. 10b). In contrast, the magmatic f_{O_2} of the IOA-related intrusive rocks increases from ΔFMQ +2.1 ± 0.3 (1σ) to ΔFMQ +2.7 ± 0.2 (1σ) with decreasing temperature (Fig. 10b).

Estimation of melt volatile concentrations

H_2O content approximation: The H_2O concentrations of the silicate melts were approximated using the amphibole hygrometer (Ridolfi, 2021). These range from 5.6 ± 1.5 to 8.8 ± 0.5 wt % (avg. = 6.3 ± 1.0 wt %, 1σ) for porphyry- and skarn-related rocks, and 4.9 ± 0.3 to 5.7 ± 0.3 wt. % (avg. = 5.2 ± 0.5 wt %, 1σ; Fig. 10c) for IOA-related rocks. Given that the standard deviation is 2.4 wt % for H_2O estimated using the amphibole hygrometer (Ridolfi, 2021), our results are consistent with the average H_2O contents in global mafic-intermediate arc magmas (4.0 ± 1.3 wt %; Rasmussen et al., 2022). The positive correlation of the crystallization pressure with melt H_2O contents (Fig. 10c) is consistent with increasing magma storage depth with melt H_2O contents (Rasmussen et al., 2022).

S-Cl contents: For porphyry- and skarn-related intrusions, the S concentrations in apatite range from 0.08 ± 0.08 to 0.28 ± 0.03 wt % (avg. = 0.13 ± 0.06 wt %; 1σ), and the Cl concentrations are from 0.09 ± 0.02 to 0.89 ± 0.29 wt % (avg. = 0.35 ± 0.28 wt %; 1σ), respectively (Table 6). The molar fractions of F, Cl, and OH and ratios of X_F/X_{OH}, X_{Cl}/X_{OH}, and X_F/X_{Cl} were used with the thermodynamic models from Stock et al. (2018) to distinguish apatite grains crystallized prior to volatile exsolution (i.e., predegassed) and after volatile exsolution (i.e., postdegassed; see App. Fig. A5). The results indicate that most apatite grains from the porphyry- and skarn-related intrusive rocks crystallized prior to volatile exsolution.

The S and Cl concentrations in igneous apatite from the IOA-related silicate melts range from 0.01 ± 0.01 to 0.11 ± 0.02 wt % (1σ) and 0.39 ± 0.26 to 2.94 ± 1.71 wt % (1σ), respectively (Table 6). The data reveal two populations of apatite in these samples, consistent with predegassed and postdegassed apatite crystallization (Fig. 11). The average S and Cl concentrations in the predegassed apatite grains in the Ningwu IOA ore district are 0.10 ± 0.01 wt % (ranging from 0.09 ± 0.06 to 0.11 ± 0.02 wt %; 1σ) and 2.22 ± 0.77 wt % (ranging

Table 5. P-T Crystallization Conditions, Magmatic f_{O_2}, and Zircon Eu/Eu* for Representative Intrusive Rocks Associated with Porphyry and Skarn Cu ± Au and Iron Oxide-Apatite Deposits in the Middle-Lower Yangtze River Metallogenic Belt, China

			P (MPa)	T (°C)		f_{O_2} (ΔFMQ)		Eu/Eu*
Sample	District	Deposit	Amp [1]	Zrn [2]	Amp [3]	Zrn [2]	Amp [3]	Zrn
DYTLS-01	Daye	Tonglushan	118 ± 30	803 ± 52	707 ± 27	2.1 ± 0.7	1.6 ± 0.2	0.56 ± 0.11
DYTSK-01	Daye	Tongshankou	198 ± 19	740 ± 32	757 ± 9	1.2 ± 0.4	1.3 ± 0.2	0.74 ± 0.07
DYHLS-01	Daye	Huanglongshan	330 ± 86	870 ± 31	810 ± 39	0.6 ± 0.5	1.9 ± 0.5	0.62 ± 0.09
DYJGZ-01	Daye	Jiguanzui	n.a.	788 ± 28^R	n.a.	1.9 ± 0.3^R	n.a.	0.55 ± 0.05^R
				933 ± 21^C		0.7 ± 0.2^C		0.43 ± 0.04^C
JRBS-z01	Daye	Baoshan	n.a.	783 ± 16	n.a.	0.5 ± 0.6	n.a.	0.67 ± 0.05
JRCMS-z01	Daye	Chengmenshan	n.a.	753 ± 39	n.a.	1.0 ± 0.3	n.a.	0.64 ± 0.06
JRDLW-z01	Jiurui	Dongleiwan	n.a.	767 ± 13	n.a.	1.7 ± 0.3	n.a.	0.65 ± 0.05
JRDJS-z01	Jiurui	Dengjiashan	n.a.	780 ± 27	n.a.	2.0 ± 0.2	n.a.	0.55 ± 0.04
JRJLS-02	Jiurui	Jilongshan	527 ± 60	765 ± 43	838 ± 42	1.6 ± 0.6	2.3 ± 0.4	0.57 ± 0.04
JRWS-z01	Jiurui	Wushan	n.a.	765 ± 88		1.9 ± 1.0		0.56 ± 0.04
GCTS-03	Guichi	Tongshan	255 ± 57	817 ± 29^R	772 ± 20	1.6 ± 0.4^R	1.8 ± 0.4	0.51 ± 0.06^R
				896 ± 10^C		0.7 ± 0.3^C		0.56 ± 0.04^C
GCMT-01	Guichi	Matou	181 ± 56	741 ± 29	749 ± 24	1.0 ± 0.5	0.9 ± 0.4	0.53 ± 0.05
AQYS-03	Guichi	Yueshan	131 ± 39	860 ± 22	735 ± 11	1.6 ± 0.3	1.5 ± 0.3	0.65 ± 0.11
TLDGS-01	Tongling	Dongguashan	352 ± 38	819 ± 36	796 ± 13	1.9 ± 0.3	1.8 ± 0.3	0.68 ± 0.08
TLHC-z01	Tongling	Hucun	n.a.	775 ± 37		2.2 ± 0.3		0.65 ± 0.04
TLHC-01	Tongling	South Hucun	178 ± 34	788 ± 26	746 ± 23	1.9 ± 0.3	1.2 ± 0.3	0.60 ± 0.06
TLJGS-z01	Tongling	Jiguanshan	n.a.	865 ± 48	n.a.	1.0 ± 0.4	n.a.	0.67 ± 0.08
TLJKL-z01	Tongling	Jinkouling	n.a.	798 ± 42^R	n.a.	2.1 ± 0.4^R	n.a.	0.70 ± 0.08^C
				920 ± 39^C		0.7 ± 0.3^C		0.61 ± 0.04^R
TLQSJ-z01	Tongling	Qingshanjiao	n.a.	840 ± 36	n.a.	1.4 ± 0.4	n.a.	0.77 ± 0.08
TLSTJ-z01	Tongling	Shatanjiao	n.a.	776 ± 39	n.a.	1.9 ± 0.4	n.a.	0.70 ± 0.06
TLTEB-z01	Tongling	Tianebaodan	n.a.	839 ± 74	n.a.	1.8 ± 0.7	n.a.	0.73 ± 0.08
TLTGS-01	Tongling	Tongguanshan	n.a.	812 ± 39	n.a.	1.8 ± 0.7	n.a.	0.62 ± 0.11
Average			252 ± 131	810 ± 50	770 ± 40	1.5 ± 0.5	1.6 ± 0.4	0.62 ± 0.08
LZNH-06	Luzong	Ninghe	n.a.	892 ± 10	n.a.	-1.4 ± 0.2	n.a.	0.48 ± 0.03
NWGC-02	Ningwu	Gaocun	n.a.	967 ± 49	n.a.	-0.8 ± 0.4	n.a.	0.44 ± 0.05
NWHSQ-01	Ningwu	Heshangqiao	85 ± 16	870 ± 28	n.a.	0.5 ± 0.3	n.a.	0.35 ± 0.03
NWHSQ-04	Ningwu	Heshangqiao	168 ± 25	941 ± 31	772 ± 17	0.1 ± 0.3	2.4 ± 0.4	0.33 ± 0.04
NWWS-02	Ningwu	Wushan	n.a.	804 ± 24	n.a.	0.6 ± 0.3	n.a.	0.53 ± 0.09
NWHMS-01	Ningwu	Hemushan	n.a.	883 ± 25	n.a.	2.1 ± 0.4	n.a.	0.34 ± 0.04
NWZJGS-02	Ningwu	Zhongjiu-Gushan	189 ± 72	875 ± 51	789 ± 42	1.2 ± 0.7	2.1 ± 0.3	0.53 ± 0.04
Average			147 ± 55	890 ± 50	750 ± 50	0.3 ± 1.2	2.4 ± 0.3	0.43 ± 0.09

Notes: The results estimated from zircon geochemistry for samples DYTLS-01, DYTS-02, DYTSK-01 and TLTGS-01 are assumed to be comparable to that for other samples collected from the same deposit; previously published zircon geochemistry data for samples from the Tonglushan, Tongshankou, Wushan, Tongguanshan, and Dongguashan deposits (Wang et al., 2013; Wang et al., 2015; Wen et al., 2020, and Zhang, J., et al., 2021) have been compiled and merged with our data to calculate the relevant values; methods in estimating P-T crystallization conditions and magmatic f_{O_2}: 1 = Mutch et al. (2016); 2 = Loucks et al. (2020); 3 = Ridolfi (2021); Eu/Eu* = $Eu_n/(Sm_n \times Gd_n)^{1/2}$; n represents chondrite-normalized; normalization data are from Sun and McDonough (1989); the letters C and R represent values estimated using samples from the core and rim, respectively

from 1.26 ± 0.03 to 2.94 ± 1.71 wt %; 1σ), respectively (Table 6). Apatite that crystallized after degassing yielded lower average S and Cl concentrations of 0.02 ± 0.01 wt % (1σ) and 1.03 ± 0.55 wt %, respectively (1σ; Table 6). In contrast, hydrothermal apatite grains in the albitized diorite sample NWHSQ-04 contain homogenous S and Cl contents of 0.16 ± 0.06 wt % (1σ) and 0.36 ± 0.07 wt % (1σ), respectively. These S and Cl concentrations are consistent with data from Zeng et al. (2016) for apatite crystallized from early-stage magmatic-hydrothermal fluids in the Ningwu ore district (Fig. 11).

The estimated average concentrations of S in the porphyry- and skarn-related and IOA-related silicate melts in equilibrium with predegassed apatite are comparable at 0.13 ± 0.06 wt % (1σ) and 0.16 ± 0.09 wt % (1σ), respectively (Fig. 12; Table 6). The average melt Cl/H_2O ratios estimated using apatite compositions for the intrusive rocks associated with the porphyry and skarn Cu and IOA deposits are 0.05 ± 0.03 (1σ) and 0.14 ± 0.02 (1σ) using the model of Li and Hermann (2017) and 0.04 ± 0.03 (1σ) and 0.11 ± 0.03 (1σ) using the model of Li and Costa (2020). Using the exchange partition coefficients of OH-Cl between amphibole and melt (Giesting and Filiberto, 2014), the melt Cl/H_2O ratios for porphyry and skarn Cu deposits are estimated to be lower than those for IOA deposits (0.02 ± 0.01 vs. 0.12 ± 0.04; 1σ; Fig. 12; Table 6). Similarly, the melt Cl/H_2O ratios estimated using biotite and bulk-rock compositions (Zhang, C., et al., 2022) are 0.03 ± 0.01 and 0.34 ± 0.03 for the porphyry- and skarn-related and IOA-related rocks, respectively (Table 6). These results are internally consistent, suggesting that the Cl/H_2O ratios of the IOA-related melts were a factor of 3 to 11 higher than those of the porphyry- and skarn-related melts.

Discussion

Magmatic oxidation states

The temperature-independent, mineral-based oxybarometers indicate that f_{O_2}, reported as ΔFMQ, varied in the source magmas that evolved ore-forming fluids for porphyry Cu de-

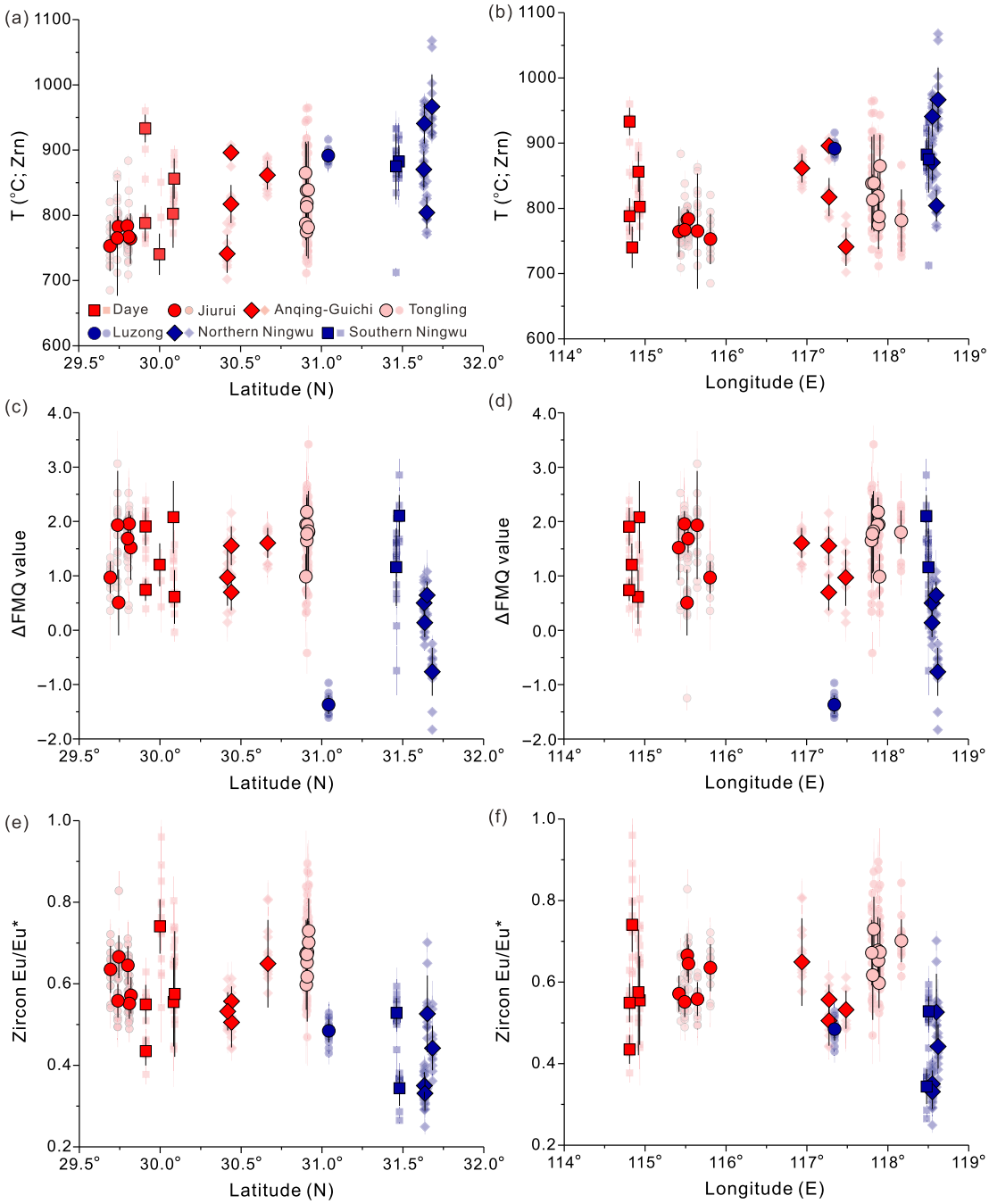

Fig. 6. (a, b) Plots of Ti-in-zircon temperature versus latitude and longitude. (c, d) Plots of ΔFMQ values versus latitude and longitude. (e, f) Plots of zircon Eu/Eu* ratios versus latitude and longitude. Small symbols in (a) and (b) are individual zircon analyses, whereas the larger ones are average values for the groups of zircon samples. Error bars represent standard deviations (1σ).

posits and IOA deposits in the Middle-Lower Yangtze River metallogenic belt (Fig. 13). The f_{O_2} data reported here for the causative magmas for the porphyry and skarn Cu ± Au deposits indicate that they were oxidized throughout their evolution (Fig. 13), consistent with published studies of arc magmas in general and those that formed porphyry Cu systems (Richards, 2015; Cottrell et al., 2021; Meng et al., 2021a; 2022). The porphyry- and skarn-related high-K calc-alkaline magmas in the Middle-Lower Yangtze River metallogenic belt are thought to have been derived from (1) thickened or delaminated lower crust (Wang et al., 2007; Hou, Z.Q., et al., 2011) or (2) partial melting of sub-arc mantle that was metasomatized in the Neoproterozoic (Li et al., 2008; Wang et al., 2016; Chen et al., 2020) and/or the Mesozoic (Mao et al., 2011). The estimated magmatic f_{O_2} values reported here discount the possibility of the former model considering that the analyzed Archean-Neoproterozoic zircon xenocrysts that are probably entrained from the Precambrian crystalline

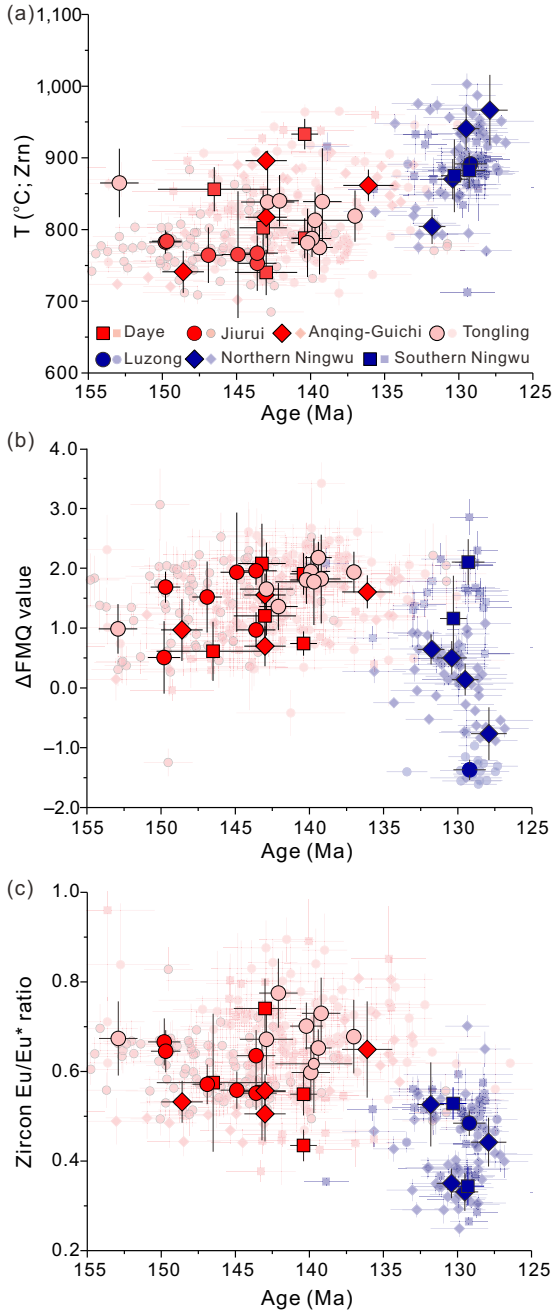

Fig. 7. Plots of (a) Ti-in-zircon temperature, (b) ΔFMQ (fayalite-magnetite-quartz) values, and (c) zircon Eu/Eu* ratios versus zircon U-Pb age for porphyry- and skarn-related and iron oxide-apatite–related igneous rocks in the Middle-Lower Yangtze River metallogenic belt. Small symbols in (a) and (b) are individual zircon analyses, whereas the larger ones are average values for the groups of zircon samples. The $^{206}Pb/^{238}U$ ages with standard deviation (1σ) are reported for the individual zircon grains, whereas the concordia or intercept ages with 2 standard errors are plotted for individual samples. Error bars for the Ti-in-zircon temperature, ΔFMQ values, and zircon Eu/Eu* ratios represent standard deviations (1σ).

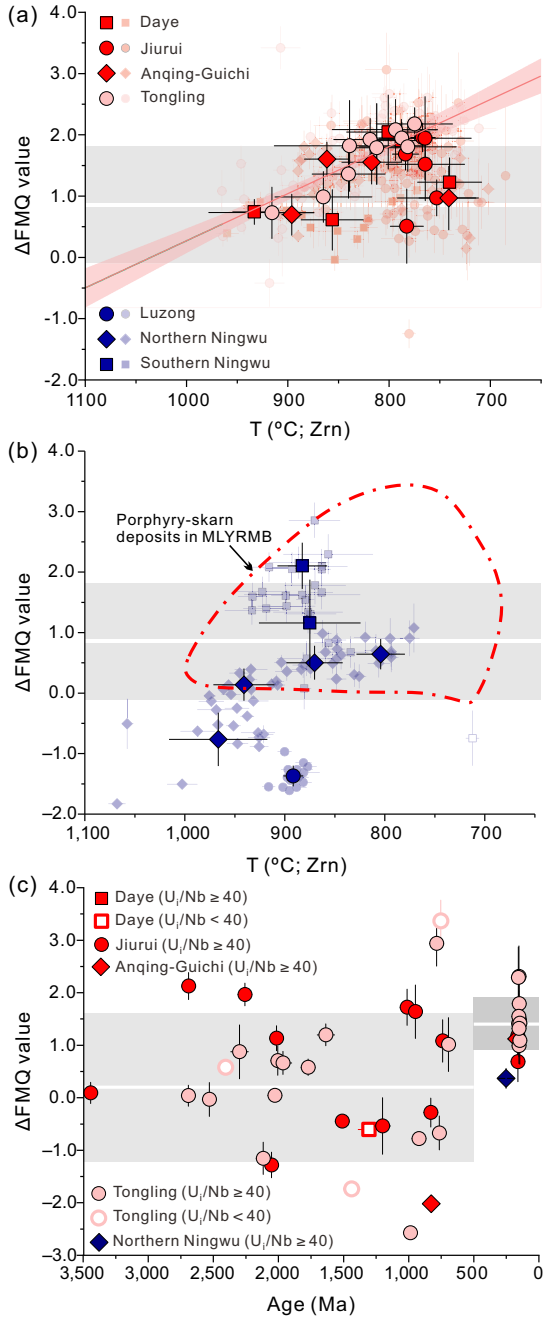

Fig. 8. (a, b) Plots of ΔFMQ (fayalite-magnetite-quartz) values versus Ti-in-zircon temperature for porphyry- and skarn- and iron oxide-apatite (IOA)-related magmas in the Middle-Lower Yangtze River metallogenic belt. (c) Plots of ΔFMQ values versus U-Pb age of the xenocrystic zircon grains in ore-related samples from the Middle-Lower Yangtze River metallogenic belt (MLYRB). The zircon oxybarometer and revised Ti-in-zircon thermometer are from Loucks et al. (2020). We assume a pressure of 200 MPa for estimating the Ti-in-zircon temperatures for both porphyry- and skarn-related and IOA-related magmas. Variation of pressure by ~100 MPa will produce errors of ~10°C, which is within the range of the standard deviations of temperature estimates (10°–90°C). Small symbols in (a) and (b) are individual zircon analyses, whereas the larger ones are average values for the groups of zircon samples. The symbols in (c) are individual analyses of xenocrystic zircon grains. Error bars represent standard deviations (1σ). The pink band in (a) represents a 95% confidence interval with the regression line in the center for the samples in Tongling ore district (R^2 = 0.76 for all the average values). The gray bands represent the average ΔFMQ value of 0.85 ± 0.95 (1σ) estimated using a zircon oxybarometer for Phanerozoic arc magmas (Meng et al., 2022).

basement are constrained to be relatively reduced (~ΔFMQ +0; Fig. 5a), so that pure remobilization of the Precambrian crystalline basement (i.e., dominated by late Archean to Paleoproterozoic tonalite-trondhjemite-granodiorite; Dong et al., 2011) and their mafic-ultramafic counterparts during

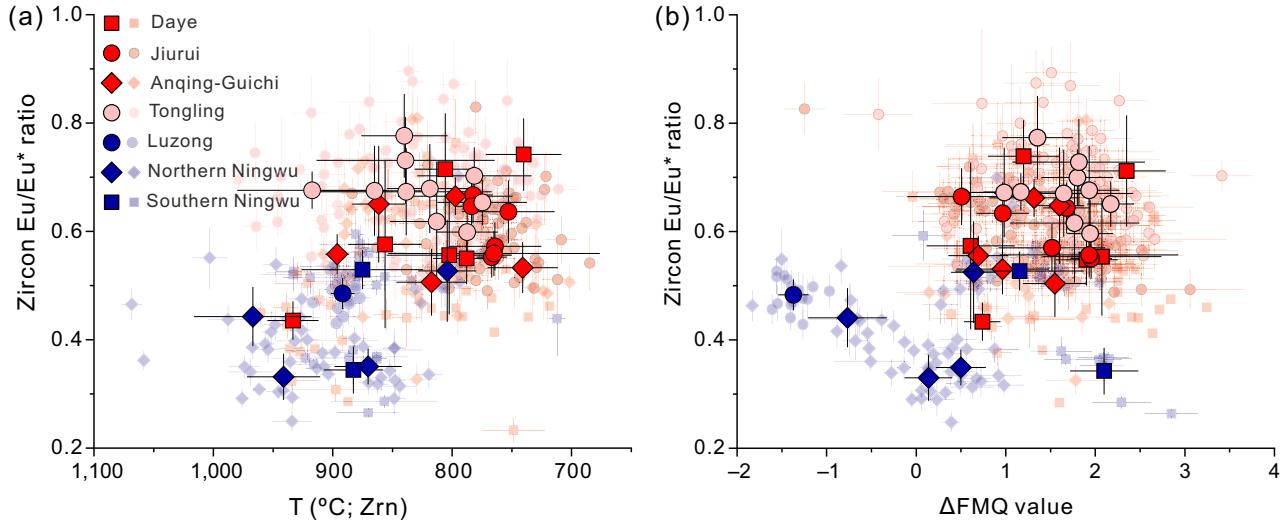

Fig. 9. Plots of zircon Eu/Eu* ratio versus (a) Ti-in-zircon temperature and (b) ΔFMQ (fayalite-magnetite-quartz) value for porphyry- and skarn- and iron oxide-apatite (IOA)-related intrusive samples from the Middle-Lower Yangtze River metallogenic belt. Small symbols are individual zircon analyses, whereas larger ones are average sample compositions. Error bars represent standard deviations (1σ).

thickening or delamination of the lower crust should have produced relatively reduced and S-poor magmas. A significant modification and oxidation of the lithospheric mantle is therefore required. Compared to the scattered ΔFMQ values (~0 on average; Fig. 8c) estimated using the compositions of the Neoproterozoic arc-like xenocrystic zircon grains (U_i/Nb ratios of ≥40; Grimes et al., 2015), the Jurassic arc-like zircon xenocrysts yielded relatively high magmatic f_{O_2} of ΔFMQ +1.4 ± 0.5 (1σ, n = 14). We therefore suggest that the fluids or melts released during the paleo-Pacific flat-slab subduction may have contributed to metasomatism and oxidation of the mantle from which the oxidized porphyry- and skarn-related magmas formed in the Middle-Lower Yangtze River metallogenic belt.

The relatively high f_{O_2} values of ΔFMQ +0.5 to ΔFMQ +2.5 for the porphyry- and skarn-related magmas predict the coexistence of sulfate and sulfide in the silicate melt by following the experimentally determined sulfide-sulfate transition in f_{O_2} space for basaltic-dacitic melt at 1,000°C and 300 MPa (Jugo et al., 2010; Botcharnikov et al., 2011; Kleinsasser et al., 2022). This is supported by the presence of magmatic sulfide and sulfate minerals in igneous rocks from the Tongling (Du and Audétat, 2020) and Daye districts (Table 3), respectively. The magmatic f_{O_2} increased with magma cooling, which may be attributed to the fractionation of Fe^{2+}-bearing minerals (Ulmer et al., 2018; Tang et al., 2018; Zhang, J.B., et al., 2022). As the magma evolved, the estimated f_{O_2} increased to ΔFMQ +2.5 at 770°C and then decreased to ~ΔFMQ +1 at ~700°C (Fig. 13).

Exsolution of magmatic-hydrothermal fluids from hydrous melts can occur during their emplacement in the upper crust (e.g., ~300 MPa; Edmonds and Woods, 2018). The decrease in f_{O_2} as the porphyry- and skarn-related magmas cooled from 800° to 700°C could be explained by mass transfer of sulfur from the melt to the exsolved magmatic-hydrothermal fluid, where sulfur in the melt at a lower temperature is predicted to be both sulfate $(SO_4)^{2-}$ and sulfide (H_2S) and sulfur in the fluid is sulfite (SO_2) at ~ΔFMQ +2.5 (Jugo et al., 2010; Audétat and Simon, 2012; Nash et al., 2019). The iron reduction and H_2S oxidation is described by the reaction:

$$3Fe_2O_3\ (\text{melt}) + H_2S\ (\text{melt}) = 6FeO\ (\text{melt}) + SO_2\ (\text{fluid}) + H_2O\ (\text{fluid}). \quad (1)$$

The f_{O_2} values for the intrusive rocks in the northern Ningwu ore district increased by nearly two orders of magnitude from ΔFMQ –1 at 970°C to ΔFMQ +0.5 at 800°C, and then increased to ΔFMQ +2.5 at <800°C (Fig. 13). The variable f_{O_2} values for the two groups of samples may be attributed to the difference in the amount of evaporite assimilated, whereas the increasing trend in f_{O_2} can be explained by fractionation of Fe^{2+}-bearing minerals and two reactions that occur during degassing of the melt that yielded high Cl/H_2O ratios. This increases the Fe^{3+}/Fe^{2+} ratio of the melt resulting in oxidation via the following reactions:

$$3FeO\ (\text{melt}) + SO_4^{2-} + 2HCl = Fe_3O_4\ (\text{melt}) + SO_2\ (\text{gas}) + 2Cl^-\ (\text{fluid}) + H_2O\ (\text{fluid}); \quad (2)$$

$$Fe_3O_4\ (\text{melt}) + 2HCl = Fe_2O_3\ (\text{melt}) + FeCl_2\ (\text{fluid}) + H_2O\ (\text{fluid}). \quad (3)$$

The latter involves the mass transfer of Fe^{2+} from the melt to the exsolved fluid phase as $FeCl_2$ (Simon et al., 2004; Bell and Simon, 2011).

Source of the volatile elements

Silicate melts that produced porphyry and skarn Cu ± Au deposits in the Middle-Lower Yangtze River metallogenic belt are distinct from those that produced the IOA deposits. The porphyry- and skarn-related melts were hydrous (~5–8 wt % H_2O) and S-rich (~0.13 ± 0.06 wt %) with moderate Cl/H_2O ratios (~0.04 ± 0.03), consistent with porphyry Cu systems and arc magmas globally (Candela and Piccoli, 1995; Meinert et al., 2005; Audétat and Simon, 2012; Richards, 2015; Meng et al., 2021a; Fig. 12). The IOA-related melts were less hydrous (~4–5 wt % H_2O), with significantly higher Cl/H_2O

Table 6. Primary Apatite S-Cl Content and Estimates of Magmatic Volatile Contents for Representative Intrusive Rocks Associated With Porphyry and Skarn Cu ± Au and Iron Oxide-Apatite Deposits in the Middle-Lower Yangtze River Metallogenic Belt, China

Sample	District	Deposit	Ap S (wt %, SD)	Ap Cl (wt %, SD)	Melt H_2O (wt %, SD) Amp[1]	Melt S (wt %, SD) Ap[2]	Melt Cl/H_2O ratio Ap[3]	Ap[4]	Bt[5]	Amp[6]
Porphyry-skarn Cu ± Au deposits										
DYTLS-01	Daye	Tonglushan	0.10 ± 0.06	0.09 ± 0.02	5.98 ± 0.38	0.05 ± 0.03	0.02 ± 0.00	0.02 ± 0.01	n.a.	0.04 ± 0.01
DYTSK-01	Daye	Tongshankou	0.09 ± 0.04^D	0.13 ± 0.03^D	5.81 ± 0.27	0.12 ± 0.05^D		0.02 ± 0.01	0.03 ± 0.00	0.01 ± 0.00
DYHLS-01	Daye	Huanglongshan	0.08 ± 0.02	0.27 ± 0.20	5.95 ± 0.57	0.16 ± 0.03	0.03 ± 0.03	0.03 ± 0.03	n.a.	0.02 ± 0.01
DYJGZ-01	Daye	Jiguanzui	0.12 ± 0.04	0.57 ± 0.60	n.a.	0.21 ± 0.07	0.13 ± 0.02	0.13 ± 0.05		n.a.
JRJLS-03	Jiurui	Jilongshan	0.16 ± 0.03	0.89 ± 0.29	8.81 ± 0.47	0.12 ± 0.02	0.07 ± 0.02	0.04 ± 0.02	0.02 ± 0.00	0.01 ± 0.00
GCTS-03	Guichi	Tongshan	0.12 ± 0.08	0.80 ± 0.08	6.40 ± 0.45	0.10 ± 0.06	0.08 ± 0.01	0.07 ± 0.01	n.a.	0.04 ± 0.01
GCMT-01	Guichi	Matou	0.10 ± 0.07^D	0.20 ± 0.07^D	5.60 ± 1.47	0.13 ± 0.10^D	0.03 ± 0.01^D	0.02 ± 0.01^D	0.04 ± 0.01	0.02 ± 0.01
AQYS-03	Guichi	Yueshan	0.13 ± 0.04	0.16 ± 0.04	5.77 ± 0.43	0.12 ± 0.04	0.02 ± 0.01	0.02 ± 0.01	n.a.	0.03 ± 0.01
TLDGS-01	Tongling	Dongguashan	0.14 ± 0.07	0.20 ± 0.09	6.94 ± 0.46	0.09 ± 0.04	0.03 ± 0.02	0.03 ± 0.03	n.a.	0.01 ± 0.00
TLHC-01	Tongling	South Hucun	0.11 ± 0.10	0.27 ± 0.04	5.72 ± 0.43	0.05 ± 0.05	0.03 ± 0.00	0.03 ± 0.01	0.05 ± 0.01	0.03 ± 0.01
TLTGS-01	Tongling	Tongguanshan	0.28 ± 0.03^P	0.46 ± 0.03^P	n.a.	0.24 ± 0.03^P	0.05 ± 0.00^P	0.04 ± 0.00^P	n.a.	n.a.
			0.08 ± 0.08^D	0.28 ± 0.05^D		0.06 ± 0.07^D	0.04 ± 0.00^D	0.03 ± 0.00^D		
Average^P			0.13 ± 0.06	0.35 ± 0.28	6.26 ± 0.99	0.13 ± 0.06	0.05 ± 0.03	0.04 ± 0.03	0.03 ± 0.01	0.02 ± 0.01
Iron oxide-apatite deposits										
NWHSQ-01	Ningwu	Heshangqiao	0.11 ± 0.02^P	2.94 ± 1.71^P	n.a.	0.25 ± 0.05^P	0.15 ± 0.05^P	0.12 ± 0.08^P	0.34 ± 0.03	0.15 ± 0.05
			0.02 ± 0.01^D	1.03 ± 0.55^D		0.04 ± 0.03^D	0.08 ± 0.04^D	0.05 ± 0.03^D		
NWWS-02	Ningwu	Wushan	0.09 ± 0.03^P	1.61 ± 0.14^P	n.a.	0.16 ± 0.06^P	0.11 ± 0.01^P	0.05 ± 0.01^P	n.a.	n.a.
			0.01 ± 0.01^D	1.07 ± 0.35^D		0.04 ± 0.03^D	0.04 ± 0.03^D	0.02 ± 0.02^D		
NWHMS-01	Ningwu	Hemushan	0.10 ± 0.12	1.26 ± 0.03	n.a.	0.04 ± 0.05	0.13 ± 0.03	0.12 ± 0.05	n.a.	n.a.
NWZJGS-02	Ningwu	Zhongjiu-Gushan	0.09 ± 0.06^P	2.33 ± 0.54^P	4.87 ± 0.19^C	0.10 ± 0.06^P	0.15 ± 0.03^P	0.14 ± 0.04^P	n.a.	0.09 ± 0.03^C
			0.02 ± 0.00^D	0.39 ± 0.26^D	5.74 ± 0.30^R	0.02 ± 0.00^D	0.04 ± 0.02^D	0.03 ± 0.01^D		0.10 ± 0.02^R
NWHSQ-04	Ningwu	Heshangqiao	0.16 ± 0.06	0.36 ± 0.07	4.95 ± 0.33	n.a.	n.a.	n.a.	n.a.	n.a.
Average^P			0.10 ± 0.01	2.22 ± 0.77	5.19 ± 0.48	0.16 ± 0.09	0.14 ± 0.02	0.11 ± 0.03	0.34 ± 0.03	0.12 ± 0.04

Notes: The subscripts against the melt H_2O and S concentrations as well as the Cl/H_2O ratios indicate the references for the estimation methods: 1 = Ridolfi (2021), 2 = Meng et al. (2021a), 3 = Li and Hermann (2017), 4 = Li and Costa (2020), 5 = Zhang, C., et al. (2022), and 6 = Giesting and Filiberto (2014); melt H_2O contents estimated using amphibole composition are regarded as semiquantitative; the symbols *P* and *D* against S-Cl contents in the apatite and melt compositions or ratios represent the predegassed and degassed compositions, respectively; they are only marked when the degassed apatite grains are identified in the samples; we assume comparable fo_2-P-T conditions at the time of apatite crystallization under predegassed and degassed conditions for the estimation; the symbols *C* and *R* against the H_2O and Cl contents (Amp) represent the values estimated using the composition of amphibole grains in the core and rim, respectively; the H_2O concentrations are regarded as semiquantitative

Abbreviations: Amp = amphibole, Ap = apatite, Bt = biotite

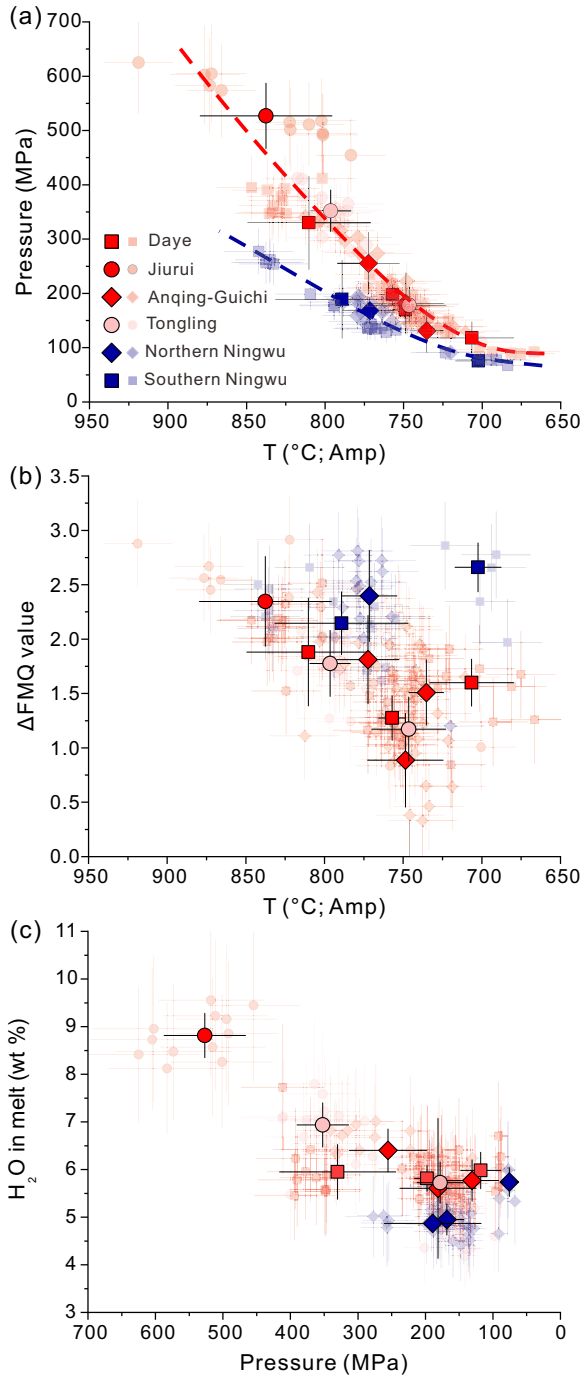

Fig. 10. Plots of pressure, temperature, ΔFMQ (fayalite-magnetite-quartz) value, and H_2O concentration estimated using amphibole composition for porphyry- and skarn- and iron oxide-apatite (IOA)-related intrusive samples in Middle-Lower Yangtze River metallogenic belt. Small symbols are individual zircon analyses, whereas larger ones are average sample compositions. Error bars represent standard deviations (1σ).

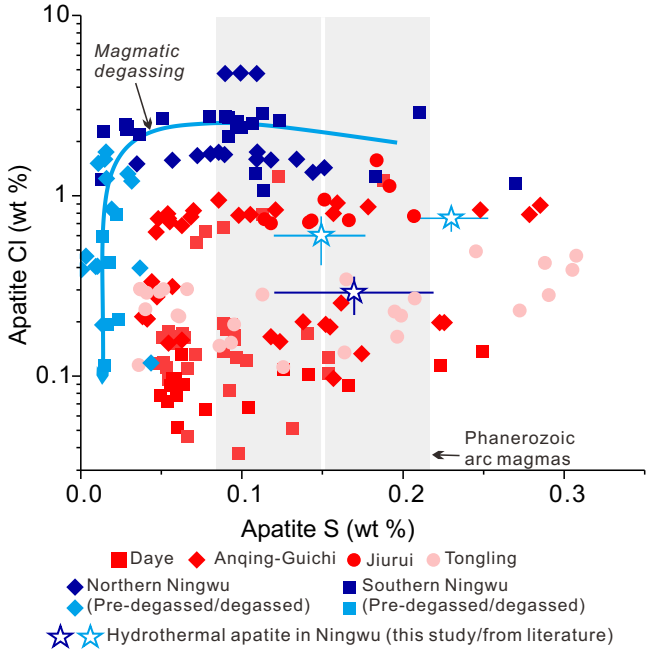

Fig. 11. Plots of S versus Cl concentration in primary apatite grains for porphyry- and skarn- and iron oxide-apatite (IOA)-related intrusive samples in the Middle-Lower Yangtze River metallogenic belt. The symbols represent individual analyses, except that the star symbols represent the average values with standard deviations for apatite grains crystallized from early-stage magmatic fluids in Ningwu ore district. The S and Cl data for the hydrothermal apatite grains in Ningwu are from Zeng et al. (2016). The average S concentrations in apatite grains for Phanerozoic arc magmas are from Meng et al. (2021a).

ratios (~0.11 ± 0.03) and highly variable S contents (<0.16 ± 0.09 wt %; Fig. 12).

The hydrous ore-forming melts for the porphyry and skarn Cu ± Au deposits lack whole-rock Eu anomalies and have elevated whole-rock Sr/Y ratios (see summary in Chen et al., 2020) and higher zircon Eu/Eu* ratios (Figs. 6–8) that are consistent with fractionation of amphibole and suppression of plagioclase (Richards and Kerrich, 2007). In comparison, the IOA-related dioritic rocks typically yielded negative whole-rock Eu anomalies, lower whole-rock Sr/Y ratios (see summary in Chen et al., 2020), and lower zircon Eu/Eu* ratios (Figs. 6–8), suggesting early fractionation of plagioclase that may be favored in the relatively dry magmas (Richards, 2011). These systematic changes in geochemical features are consistent with lithospheric extension at ~135 Ma (Figs. 2, 14; Li et al., 2019).

Exhaustion of the volatile ingredients in the previously metasomatized mantle source without a continuous flux of oxidized slab-derived fluids is not capable of maintaining the S contents in the derivative silicate melts because reduced sulfur will be separated early from the magmas as sulfide liquid (Wallace and Edmonds, 2011; Richards et al., 2017; Meng et al., 2022). Slab-derived fluids typically yielded high Cl/H_2O ratios, and the decline in the slab-derived flux to the mantle (e.g., during slab rollback or remobilization of previously metasomatized mantle for the Middle-Lower Yangtze River metallogenic belt) will decrease the Cl/H_2O ratios in the derivative melts (Kent et al., 2002; Candela and Piccoli, 2005). However, the predegassed S concentrations in ore-forming melts for the porphyry and skarn Cu ± Au deposits are indistinguishable from those in the magmas associated with IOA deposits, whereas the Cl/H_2O ratios of the predegassed IOA-related melts estimated using apatite compositions are a factor of ~3 higher than those estimated for porphyry- and

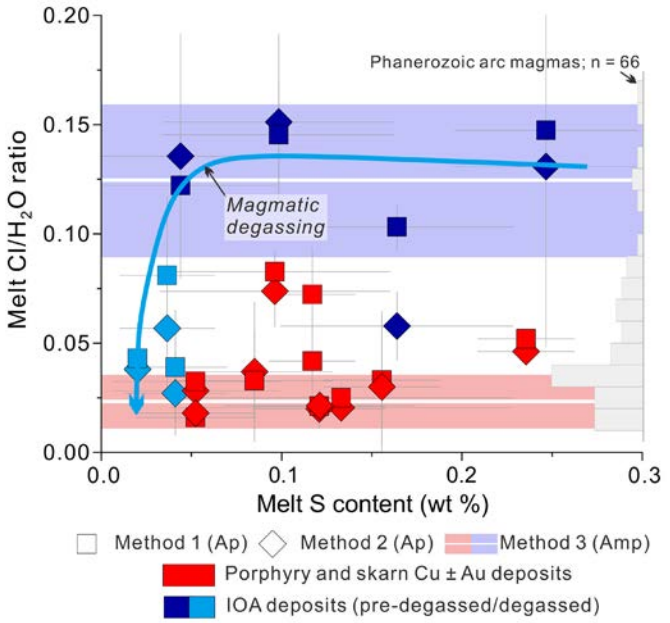

Fig. 12. Plots of S versus Cl/H_2O ratios for the silicate melts related to porphyry and skarn Cu and iron oxide-apatite (IOA) deposits in the Middle-Lower Yangtze River metallogenic belt. Method 1 = Li and Hermann (2017); Method 2 = Li and Costa (2020); Method 3 = Giesting and Filiberto (2014). The estimated Cl/H_2O ratios of the silicate melts using apatite and amphibole compositions are consistent with uncertainty. Note that the Cl/H_2O ratios of the degassed IOA-related melts may represent the maximum values if we assume that the degassed apatite grains crystallized at a lower temperature compared to those predegassed grains. The Cl/H_2O result estimated using biotite and whole-rock compositions (Zhang, S., et al., 2021) for one sample of IOA-related dioritic rock has been reported in the main text but is not plotted here. The measured Cl/H_2O ratios for melt inclusions in olivine and minor pyroxene from Phanerozoic arc rocks ($SiO_2 \geq 52$ wt %; from GEOROC database) were plotted in the histogram, in which the melt inclusion data were filtered using $CO_2 \geq 50$ ppm to minimize the effect of magmatic degassing. One sample with Cl/H_2O ratio of 0.40 was not plotted. N represents numbers of the groups of melt inclusions. Abbreviations: Amp = amphibole, Ap = apatite.

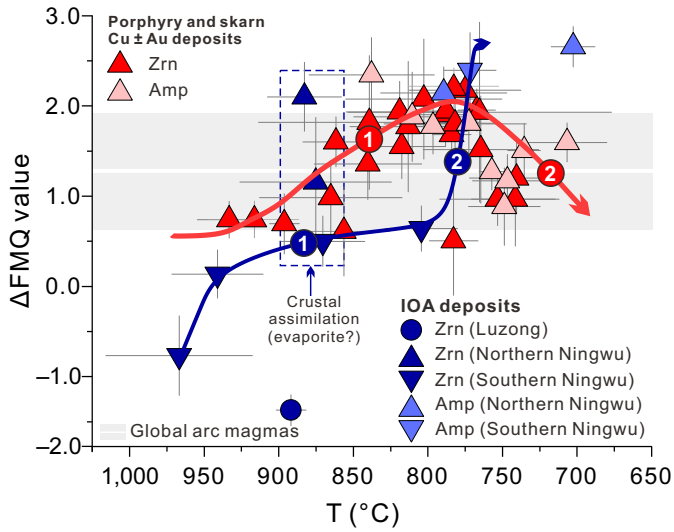

Fig. 13. Summary of ΔFMQ (fayalite-magnetite-quartz) values and temperatures estimated for porphyry- and skarn- and iron oxide-apatite (IOA)-related intrusive rocks from the Middle-Lower Yangtze River metallogenic belt. Error bars represent standard deviations (1σ). The gray band represents the average f_{O_2} value estimated using magnetite-ilmenite mineral pairs for global arc magmas (Cottrell et al., 2022). See the explanation for the trajectories in the main text. Abbreviations: Amp = amphibole, Zrn = zircon.

skarn-related melts and those for most Phanerozoic arc magmas (Fig. 12). We therefore suggest that an additional source with a higher S concentration and Cl/H_2O ratio is required for forming IOA-related melts (Fig. 14).

One possible source to explain the S- and Cl-rich nature of the predegassed silicate melts associated with IOA deposits is the assimilation of evaporite sequences. This is supported by (1) the presence of hypersaline brine inclusions hosted in pyroxene-garnet skarns in the Ningwu basin (Li, W., et al., 2015), in which the brine inclusions are SO_4-rich (3–39 wt %) and have Cl/Br, Na/K, and Na/B ratios consistent with the assimilation of sedimentary halite (Li, W., et al., 2015), and (2) the heavy sulfur isotope values in hydrothermal anhydrite ($\delta^{34}S_{Anh}$ = +15.2 to +16.9‰) and pyrite ($\delta^{34}S_{Py}$ = +4.6 to +12.1‰; Li, W., et al., 2015; Duan et al., 2021). The hypersaline brine inclusions were trapped at temperatures of ~740° to 860°C (Ma et al., 2006; Li, W., et al., 2015), whereas the hydrothermal anhydrite and pyrite precipitated from the ore fluid at 450° to 540°C (Duan et al., 2021). The results indicate that assimilation of the evaporite sequences probably occurred before saturation of apatite at 871° ± 31°C during IOA magma crystallization (App. Fig. A6). The significantly low sulfur isotope values for the high-K calc-alkaline intrusive rocks and sulfide minerals ($\delta^{34}S$ = –2 to +5‰) from most of the studied porphyry and skarn Cu ± Au deposits suggest much stronger assimilation of evaporite sequences (as suggested by the high pyrite $\delta^{34}S$ = +4.6 to + 12.1‰) during formation of the IOA deposits rather than porphyry and skarn Cu ± Au deposits (Pan and Dong, 1999; Li, W., et al., 2015; Zhou et al., 2015; Fan et al., 2019; Duan et al., 2021).

Tectonic and metallogenic models for porphyry Cu and IOA deposits in the Middle-Lower Yangtze River metallogenic belt

Porphyry Cu and IOA systems preferentially formed under broadly compressional and extensional environments, respectively, in response to the secular tectonic evolution in subduction-related settings (Sillitoe, 2003; Mao et al., 2011; Richards et al., 2017). The tectonic setting of the Middle-Lower Yangtze River metallogenic belt at >135 Ma has been debated, with subduction and intraplate models being proposed (Table 1). The interpreted broadly compressional setting at >135 Ma, which was a common feature in eastern China and adjacent countries (e.g., Korea, Japan, and northern Vietnam; Mao et al., 2021), is incompatible with the intraplate model in which the magmas associated with porphyry and skarn Cu ± Au deposits are thought to be derived mainly from partial melting of the previously metasomatized mantle (e.g., in the Neoproterozoic) in an extensional environment (Table 1). Neoproterozoic magmatism has barely been identified in the northeastern Yangtze craton, along which the Middle-Lower Yangtze River metallogenic belt formed (Zhou et al., 2002). The scattered and low ΔFMQ values of ~0 on average (Fig. 8c) estimated from the Neoproterozoic zircon xenocrysts of

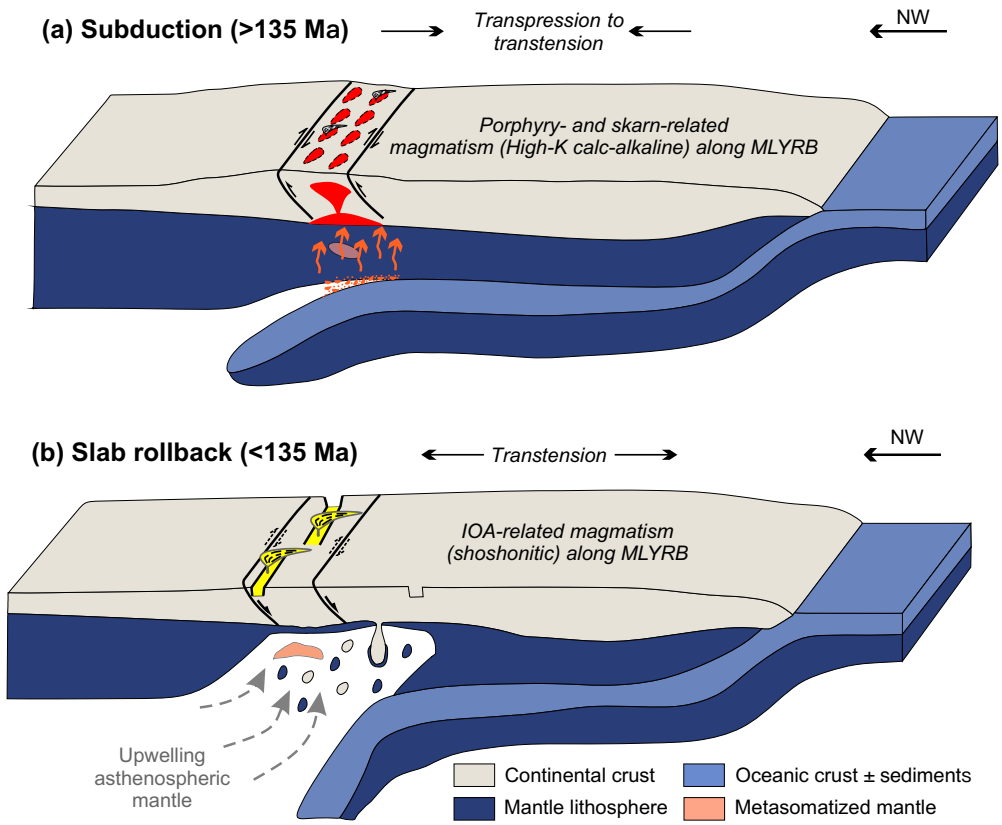

Fig. 14. Schematic cartoon models illustrating the tectonic evolution of the paleo-Pacific flat slab subduction in eastern China for the Late Jurassic-Early Cretaceous Middle-Lower Yangtze River metallogenic belt (MLYRB not to scale; adapted from Wu et al., 2019). (a) Flat-slab subduction for forming porphyry and skarn-related magmatism. (b) Slab rollback for iron oxide-apatite (IOA)-related shoshonitic rocks. The Eastern Asian continental crust is significantly simplified due to its complexity in the crystalline basement and for revealing the contrasting tectonic control on the mineralization in Middle-Lower Yangtze River metallogenic belt.

arc affinity are inconsistent with the relatively oxidized conditions of the mantle source of the Middle-Lower Yangtze River metallogenic belt in the Neoproterozoic. In contrast, the magmatic f_{O_2} data presented in this study suggest that the mantle source may have been metasomatized and oxidized since ~170 Ma, coincident with the operation of the previously proposed paleo-Pacific flat-slab subduction (Li et al., 2019; Wu et al., 2019; Liu et al., 2021; Qiu et al., 2023). The temporal coincidence suggests that the paleo-Pacific flat-slab subduction should have contributed to the oxidation of the mantle lithosphere. The long distance (~1,000 km) of the paleo-Pacific flat-slab subduction is comparable to the Farallon flat slab during the Laramide orogeny in North America (Liu, L., et al., 2010; Axen et al., 2018; Yan et al., 2020). Fluids and/or melts released from the paleo-Pacific oceanic plate may have infiltrated, weakened, and triggered the partial melting of the overlying mantle lithosphere to produce adakitic magmas that ascend along suture zones (Fig. 14).

A simple model is put forward here to accommodate the tectonomagmatic evolution at the time of porphyry and skarn Cu ± Au and IOA deposit formation in the Middle-Lower Yangtze River metallogenic belt (Figs. 14, 15). Under a transpressional (or in transition to transtensional) setting (Table 1), primitive basaltic magmas were produced by partial melting of the relatively oxidized sub-arc mantle previously metasomatized by slab-derived fluids released from paleo-Pacific flat slab (Fig. 14a). Hot, hydrous basaltic magmas interacted with the upper plate lithosphere (e.g., Archean to Neoproterozoic crystalline basement) and underwent melting, assimilation, storage, and homogenization (Hildreth and Moorbath, 1988). These processes are commonly associated with the fractionation of mafic minerals and will progressively make the relatively oxidized primitive arc magmas geochemically evolved, more oxidized, and enriched in volatile elements such as H_2O and S, as well as variable Cl concentrations (Richards et al., 2012; Loucks, 2021). A moderately compressional setting inhibits rapid magma ascent (Watanabe et al., 1999) and favors the accumulation of andesitic-dacitic magmas in mid- to upper-crustal reservoirs, followed by exsolution of magmatic-hydrothermal fluids upon further cooling and interaction with the preexisting igneous or carbonate rocks to form porphyry and skarn Cu deposits (Richards, 2003; Sillitoe, 2010; Cooke et al., 2014).

Rollback of the paleo-Pacific flat slab from ~135 Ma may have led to an extensional to transtensional setting of the upper plate lithosphere in the Middle-Lower Yangtze River metallogenic belt during IOA formation (Figs. 14, 15; Table 1; Chang et al., 1991, 2012; Mao et al., 2006, 2011; Li et al., 2019) and caused a decrease in the mass transfer of aqueous fluids from the subducting slab to the mantle wedge that reduced the Cl and S in the source magmas. Upwelling metaso-

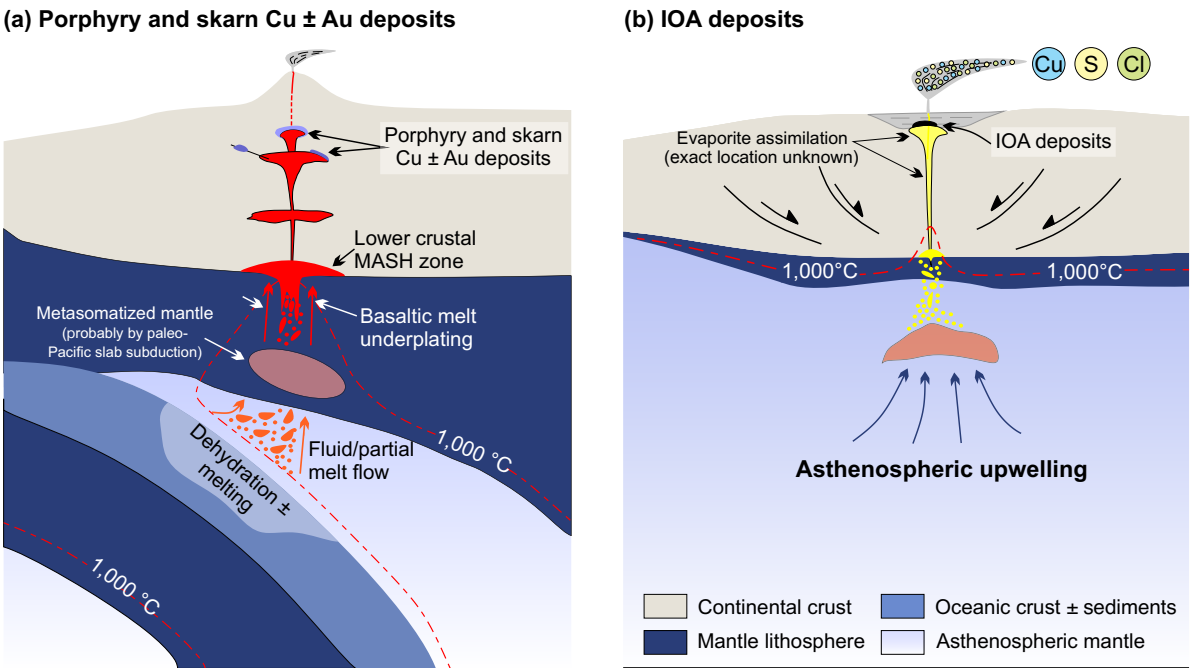

Fig. 15. Schematic cartoon models illustrating the contrasting formation modes for porphyry and skarn Cu ± Au and iron oxide-apatite (IOA) deposits in the Middle-Lower Yangtze River metallogenic belt (not to scale). Lithospheric delamination could occur at the time of IOA formation (not depicted). Abbreviation: MASH = melting, assimilation, storage, homogenization.

matized asthenosphere mantle may have interacted with the base of the crust, but the flux of hot, less-hydrous primitive basaltic magmas cannot be maintained at the base of the crust for extensive interaction, making the derivative magmas relatively mafic and less hydrous, so that they could ascend rapidly to the upper crust or erupt at the surface (Loucks, 2021), as evidenced by the voluminous volcanic deposits along the Middle-Lower Yangtze River metallogenic belt (Figs. 1, 14b, 15b). The Cl enrichment in the intermediate to mafic source magmas for IOA deposits during evaporite assimilation resulted in the mass transfer of significant quantities of Fe from the silicate melt to the exsolved ore fluid (Simon et al., 2004; Reich et al., 2022). Normal faulting networks developed in extensional settings during slab rollback can serve as conduits for the highly focused ascent of $FeCl_2$-rich magmatic-hydrothermal fluids (Fig. 15b; Reich et al., 2022). Magnetite will precipitate during the rapid ascent of an evolved magmatic-hydrothermal fluid via a reaction such as the following:

$$3FeCl_2\,(\text{fluid}) + 4H_2O\,(\text{fluid}) = Fe_3O_4\,(\text{solid}) + 6HCl\,(\text{fluid}) + H_2\,(\text{gas}) \quad (4)$$

because the solubility of $FeCl_2$ is strongly pressure dependent (Chou and Eugster, 1977; Boctor et al., 1980; Simon et al., 2004; Zajacz et al., 2008; Reich et al., 2022). The P-T paths estimated using amphibole compositions (Fig. 10a) are consistent with the steeper geotherms of extensional settings as opposed to those for arc settings (Hopkins et al., 2008). Owing to a steep geothermal gradient in the extensional setting (Richards and Mumin, 2013b), as well as to thermal convection during asthenospheric upwelling, the high-heat–producing plutons may develop high-temperature alteration zones extensively in their apical parts for the IOA deposit formation (Figs. 14b, 15b; Table 1).

The data reported here indicate that the silicate melts for porphyry and skarn Cu ± Au deposits and IOA deposits have similar predegassed S contents. However, early volatile exsolution in the IOA-related magmas, as monitored by apatite composition (Fig. 11), would emit S, H_2O, and volatile metals (e.g., Cu) to the surface (Edmonds et al., 2022) at the time of magnetite precipitation at 500° to 800°C (Reich et al., 2022; Zeng et al., 2022). The concomitant emission of S, H_2O, and Cu with Cl would limit the residual melts for large-scale Fe ± Cu sulfide mineralization at ~400°C owing to SO_2 disproportionation (Rye, 1993). We here suggest that tectonic-driven processes are the best possible explanation for the different modes for IOA versus porphyry and skarn Cu ± Au deposits in the Middle-Lower Yangtze River metallogenic belt.

Conclusions

The petrogenetic studies presented here on the ore-forming source magmas for the representative porphyry and skarn Cu ± Au and IOA deposits in the Middle-Lower Yangtze River metallogenic belt suggest that their magmatic f_{O_2} values vary systematically with crustal assimilation, crystal fractionation, and magmatic degassing. Because the estimated predegassed S concentrations are indistinguishable, the contrasting S concentrations in the primitive magmas were not the fundamental cause for the contrasting metal endowments in the porphyry and skarn Cu ± Au and IOA deposits of the Middle-Lower Yangtze River metallogenic belt. Instead, the magma composition and evolution paths (e.g., assimilation, decompression, cooling, and degassing) controlled by kinematic settings and geothermal gradients in the upper plate lithosphere exerted a first-order control on forming porphyry and skarn Cu ± Au and IOA deposit types in the Middle-Lower Yangtze River metallogenic belt.

The coexistence of an IOA deposit and a porphyry Cu system is rare on a global scale, such as in the Middle-Lower Yangtze River metallogenic belt, the Coastal Cordillera of northern Chile and Peru, and northern Sweden. Although slab rollback or retreating, asthenospheric upwelling, and extensional settings commonly follow compressional settings related to normal subduction, the IOA deposits are only rarely identified where evaporite sequences are identified or inferred based on geochemical evidence. This observation predicts that evaporite assimilation is probably a key ingredient for IOA deposit formation under a broadly extensional setting.

Data Availability

The data underlying this article are available in the article and its online supplementary materials. The supplementary materials include six appendix figures (App. Figs. A1–A6) and six appendix tables (App. Tables A1–A6).

Competing Interest Statement

The authors declare no competing interests.

Funding

The research was supported by the National Natural Science Foundation of China (Grant # 41820104010, J.M.); the U.S. National Science Foundation EAR (Grants 2214119 and 2233425, A.C.S.); a start-up research grant from China University of Geosciences (Beijing) to X. Meng (#3-8-2023-008); and a grant from the Natural Science Foundation of Anhui Province (#2208085QD111) to one of the co-authors (Shi, K).

Acknowledgments

We appreciate the field assistance from our colleagues at many institutions, including the First Brigade of the Hubei Geological Bureau (D.Q. Liu, L.Wang, and Y.D. Ruan), the Northwestern Brigade of the Jiangxi Geological Bureau (X.Z. Chen, D.B. Kong, D.S. Feng), the Geological Survey of Anhui Province (Z.T. Li) and 324 Brigade of Bureau of Geology and Mineral Exploration of Anhui Province (Y.S. Zhu), China University of Geosciences (Beijing; Y.L. Jin, Y.X. Zhang), the Institute of Mineral Resources of CAGS (Q.Q. Zhu), and the University of Science and Technology of China (Y. Wang), as well as those from the mining companies including Tongling Nonferrous Metals Group. Co., Ltd. (S. Wu) and the Nanshan Mine Company of the Maanshan Iron and Steel Group Incorporation (C.L. Wang and B.Y. Yang). We thank Z.Y. Chen, X.D. Chen, and C.H. Liu at the Mineral Institute of Mineral Resources (CAGS) for assistance with electron probe microanalyses. The graduate students, including J.H. Wang, Y. Zheng, H.X. Zhang, and J.W. Xiao, are appreciated for their assistance with LA-ICP-MS zircon isotope and trace element analyses at the China University of Geosciences (Wuhan). We sincerely thank D. Cooke, H. Chen, and an anonymous reviewer for detailed reviews that significantly improved the manuscript.

REFERENCES

Audétat, A., and Simon, A., 2012, Magmatic controls on porphyry copper genesis: Society of Economic Geologists Special Publication, v. 16, p. 553–572.

Axen, G.J., van Wijk, J.W., and Currie, C.A., 2018, Basal continental mantle lithosphere displaced by flat-slab subduction: Nature Geoscience, v. 11, p. 961–964.

Barton, M., 2013, Iron oxide (-Cu-Au-REE-P-Ag-U-Co) systems: Geochemistry of Mineral Deposits, Elsevier Inc., v. 13, p. 515–541.

Bell, A.S., and Simon, A., 2011, Experimental evidence for the alteration of the $Fe^{3+}/\Sigma Fe$ of silicate melt caused by the degassing of chlorine-bearing aqueous volatiles: Geology, v. 39, p. 499–502.

Bell, E.A., Boehnke, P., and Harrison, T.M., 2016, Recovering the primary geochemistry of Jack Hills zircons through quantitative estimates of chemical alteration: Geochimica et Cosmochimica Acta, v. 191, p. 187–202.

Boctor, N.Z., Popp, R.K., and Frantz, J.D., 1980, Mineral-solution equilibria—IV. Solubilities and the thermodynamic properties of $FeCl_2$ in the system Fe_2O_3-H_2-H_2O-HCl: Geochimica et Cosmochimica Acta, v. 44, p. 1509–1518.

Botcharnikov, R.E., Linnen, R.L., Wilke, M., Holtz, F., Jugo, P.J., and Berndt, J., 2011, High gold concentrations in sulphide-bearing magma under oxidizing conditions: Nature Geoscience, v. 4, p. 112–115.

Candela, P., and Piccoli, P., 1995, Model ore-metal partitioning from melts into vapor and vapor/brine mixtures: Mineralogical Association of Canada, Short Course Notes, v. 23, p. 101–128.

Candela, P.A., and Piccoli, P.M., 2005, Magmatic processes in the development of porphyry-type ore systems: Economic Geology, 100th Anniversary Volume, p. 25–37.

Cao, Y., Zheng, Z., Du, Y., Gao, F., Qin, X., Yang, H., Lu, Y., and Du, Y., 2017, Ore geology and fluid inclusions of the Hucunnan deposit, Tongling, Eastern China: Implications for the separation of copper and molybdenum in skarn deposits: Ore Geology Reviews, v. 81, p. 925–939.

Chang, Y.F., Liu, X.P., and Wu, Y.C., 1991, The copper-iron belt of the lower and middle reaches of the Changjiang river: Beijing, Geological Publishing House, 379 p., (in Chinese with English abstract).

Chang, Y.F., Zhou, T.F., and Fan, Y., 2012, Polygenetic compound mineralization and tectonic evolution: Study in the Middle-Lower Yangtze River Valley metallogenic belt: Acta Petrologica Sinica, v. 28, p. 3067–3075 (in Chinese with English abstract).

Chen, L., Zheng, Y.F., and Zhao, Z.F., 2020, Origin of arc-like magmatism at fossil convergent plate boundaries: Geochemical insights from Mesozoic igneous rocks in the Middle to Lower Yangtze Valley, South China: Earth-Science Reviews, v. 211, article 103416.

Chen, Y.J., and Li, N., 2009, Nature of ore-fluids of intracontinental intrusion-related hypothermal deposits and its difference from those in island arcs: Acta Petrologica Sinica, v. 25, p. 2477–2508.

Chou, I.M., and Eugster, H.P., 1977, Solubility of magnetite in supercritical chloride solutions: American Journal of Science, v. 277, p. 1296–1314.

Cooke, D.R., Hollings, P., and Walsh, J.L., 2005, Giant porphyry deposits: Characteristics, distribution, and tectonic controls: Economic Geology, v. 100, p. 801–818.

Cooke, D.R., Hollings, P., Wilkinson, J.J., and Tosdal, R.M., 2014, Geochemistry of porphyry deposits, *in* Holland, H.D., and Turekian, K.K., eds., Treatise on geochemistry, 2nd ed., v. 13: Oxford, Elsevier, p. 357–381.

Corfu, F., Hanchar, J.M., Hoskin, P.W., and Kinny, P., 2003, Atlas of zircon textures: Reviews in Mineralogy and Geochemistry, v. 53, p. 469–500.

Cottrell, E., Birner, S.K., Brounce, M., Davis, F.A., Waters, L.E., and Kelley, K.A., 2022, Oxygen fugacity across tectonic settings: American Geophysical Union, Geophysical Monograph 226, p. 33–61.

Dilles, J.H., Kent, A.J.R., Wooden, J.L., Tosdal, R.M., Koleszar, A., Lee, R.G., and Farmer, L.P., 2015, Zircon compositional evidence for sulfur-degassing from ore-forming arc magma: Economic Geology, v. 110, p. 241–251.

Dong, S., Ma, L., Liu, G., Xue, H., Shi, W., and Li, J., 2011, On dynamics of the metallogenic belt of Middle-Lower reaches of Yangtze River, eastern China: Acta Geologica Sinica, v. 85, p. 612–625 (in Chinese with English abstract).

Du, J., and Audétat, A., 2020, Early sulfide saturation is not detrimental to porphyry Cu-Au formation: Geology, v. 48, p. 519–524.

Duan, C., Li, Y., Mao, J., Hou, K., Wang, C., Yang, B., Wang, Q., and Li, W., 2019, Ore formation at the Washan iron oxide-apatite deposit in the Ningwu Ore District, eastern China: Insights from in situ LA-ICP-MS magnetite trace element geochemistry: Ore Geology Reviews, v. 112, article 103064.

Duan, C., Li, Y., Mao, J., Wang, C., Yang, B., Hou, K., Wang, Q., and Li, W., 2017, Study on the ore-forming process of the Heshangqiao IOA deposit in the Ningwu ore district: Insight from magnetite LA-ICP-MS in-situ analysis data: Acta Petrologica Sinica, v. 33, p. 3471–3483 (in Chinese with English abstract).

Duan, C., Li, Y., Mao, J., Zhu, Q., Xie, G., Wan, Q., Jian, W., and Hou, K., 2021, The role of evaporite layers in the ore-forming processes of iron

oxide-apatite and skarn Fe deposits: Examples from the middle-lower Yangtze River metallogenic Belt, east China: Ore Geology Reviews, v. 138, article 104352.
Edmonds, M., and Woods, A.W., 2018, Exsolved volatiles in magma reservoirs: Journal of Volcanology and Geothermal Research, v. 368, p. 13–30.
Edmonds, M., Mason, E., and Hogg, O., 2022, Volcanic outgassing of volatile trace metals: Annual Review of Earth and Planetary Sciences, v. 50, p. 79–98.
Fan, Y., Chang, Y.F., Zhou, T.F., Wang, S.W., Li, J.H., Li, S.Y., Chen, A.G., and Song, C.Z., 2019, Geology of mineral deposits in China: Middle-Lower Yangtze River: China Geological Publishing House, 303 p. (in Chinese).
Ferry, J.M., and Watson, E.B., 2007, New thermodynamic models and revised calibrations for the Ti-in-zircon and Zr-in-rutile thermometers: Contributions to Mineralogy and Petrology, v. 154, p. 429–437.
Giesting, P.A., and Filiberto, J., 2014, Quantitative models linking igneous amphibole composition with magma Cl and OH content: American Mineralogist, v. 99, p. 852–865.
Goldfarb, R.J., Mao, J.W., Qiu, K.F., and Goryachev, N., 2021, The great Yanshanian metallogenic event of eastern Asia: Consequences from one hundred million years of plate margin geodynamics: Gondwana Research, v. 100, p. 223–250.
Grimes, C.B., Wooden, J.L., Cheadle, M.J., and John, B.E., 2015, "Fingerprinting" tectono-magmatic provenance using trace elements in igneous zircon: Contributions to Mineralogy and Petrology, v. 170, p. 1–46.
Groves, D.I., Condie, K.C., Goldfarb, R.J., Hronsky, J.M.A., and Vielreicher, R.M., 2005, Secular changes in global tectonic processes and their influence on the temporal distribution of gold-bearing mineral deposits: Economic Geology, v. 100, p. 203–224.
Groves, D.I., Bierlein, F.P., Meinert, L.D., and Hitzman, M.W., 2010, Iron oxide copper-gold (IOCG) deposits through Earth history: Implications for origin, lithospheric setting, and distinction from other epigenetic iron oxide deposits: Economic Geology, v. 105, p. 641–654.
Gu, H., Yang, X., Nie, Z., Deng, J., Duan, L., Hu, Q., Abdul Shakoor, M., Gao, E., and Jasmi Hafiz, A.A., 2018, Study of late-Mesozoic magmatic rocks and their related copper-gold-polymetallic deposits in the Guichi ore-cluster district, Lower Yangtze River Metallogenic Belt, east China: International Geology Review, v. 60, p. 1404–1434.
Han, C.S., and Zhong, G.X., 2013, Geological characteristics and genesis of Shatanjiao ore field in Tongling ore district, Anhui: Journal of Hefei University of Technology, v. 36, p. 1504–1510 (in Chinese with English abstract).
He, Z., Zhang, X., Deng, X., Hu, H., Li, Y., Yu, H., Archer, C., Li, J., and Huang, F., 2020, The behavior of Fe and S isotopes in porphyry copper systems: Constraints from the Tongshankou Cu-Mo deposit, eastern China: Geochimica et Cosmochimica Acta, v. 270, p. 61–83.
Hildreth, W., and Moorbath, S., 1988, Crustal contributions to arc magmatism in the Andes of central Chile: Contributions to Mineralogy and Petrology, v. 98, p. 455–489.
Hopkins, M., Harrison, T.M., and Manning, C.E., 2008, Low heat flow inferred from >4 Gyr zircons suggests Hadean plate boundary interactions: Nature, v. 456, p. 493–498.
Hou, T., Zhang, Z., and Kusky, T., 2011, Gushan magnetite-apatite deposit in the Ningwu basin, Lower Yangtze River Valley, SE China: Hydrothermal or Kiruna-type?: Ore Geology Reviews, v. 43, p. 333–346.
Hou, Z.Q., Zhang, H.R., Pan, X.F., and Yang, Z.M., 2011, Porphyry Cu (–Mo–Au) deposits related to melting of thickened mafic lower crust: Examples from the eastern Tethyan metallogenic domain: Ore Geology Reviews, v. 39, p. 21–45.
Jia, L.Q., Xu, W.Y., Yang, D., Mo, X.X., Yang, Z.S., Chen, W.S., and Wang, L., 2015a, Fluid inclusion characteristics and stable isotope geochemistry of the Dongleiwan skarn Cu polymetallic deposit in the Jiujiang-Ruichang metallogenic area, Jiangxi Province: Acta Petrologica et Mineralogica, v. 34, p. 184–204 (in Chinese with English abstract).
Jia, L.Q., Xu, W.Y., Yang, D., Yang, Z.S., and Wang, L., 2015b, Zircon U-Pb and molybdenite Re-Os dating of Baoshan porphyry Cu polymetallic deposit in Jiujiang-Ruichang ore concentration area of Jiangxi Province and its geological significance: Mineral Deposits, v. 34, p. 63–80 (in Chinese with English abstract).
Jugo, P.J., Wilke, M., and Botcharnikov, R.E., 2010, Sulfur K-edge XANES analysis of natural and synthetic basaltic glasses: Implications for S speciation and S content as a function of oxygen fugacity: Geochimica et Cosmochimica Acta, v. 74, p. 5926–5938.
Kent, A.J., Peatea, D.W., Newmanb, S., Stolperb, E.M., and Pearce, J.A., 2002, Chlorine in submarine glasses from the Lau basin: Seawater contamination and constraints on the composition of slab-derived fluids: Earth and Planetary Science Letters, v. 202, p. 361–377.
Kesler, S.E., and Simon, A.C., 2015, Mineral resources, economics and the environment: Cambridge University Press, 446 p.
Kleinsasser, J.M., Simon, A.C., Konecke, B.A., Kleinsasser, M.J., Beckmann, P., and Holtz, F., 2022, Sulfide and sulfate saturation of dacitic melts as a function of oxygen fugacity: Geochimica et Cosmochimica Acta, v. 326, p. 1–16.
Konecke, B.A., Fiege, A., Simon, A.C., Linsler, S., and Holtz, F., 2019, An experimental calibration of a sulfur-in-apatite oxybarometer for mafic systems: Geochimica et Cosmochimica Acta, v. 265, p. 242–258.
Li, G., Qin, K., Song, G., and Bagas, L., 2017, The oldest Mo porphyry mineralization in the Yangtze Valley metallogenic belt of eastern China: Constraints on its origin from geochemistry, geochronology and fluid inclusion studies at Matou: Ore Geology Reviews, v. 91, p. 491–508.
Li, H.J., and Hermann, J., 2017, Chlorine and fluorine partitioning between apatite and sediment melt at 2.5 GPa, 800°C: A new experimentally derived thermodynamic model: American Mineralogist, v. 102, p. 580–594.
Li, J., Zhang, Y., Dong, S., and Johnston, S.T., 2014, Cretaceous tectonic evolution of South China: A preliminary synthesis: Earth Science Reviews, v. 134, p. 98–136.
Li, J.W., Zhao, X.F., Zhou, M.F., Vasconcelos, P., Ma, C.Q., Deng, X.D., Souza, Z.S., Zhao, Y.X., and Wu, G., 2008, Origin of the Tongshankou porphyry-skarn Cu-Mo deposit, eastern Yangtze craton, eastern China: Geochronological, geochemical, and Sr-Nd-Hf isotopic constraints: Mineralium Deposita, v. 43, p. 315–336.
Li, J.W., Vasconcelos, P., Zhou, M.F., Deng, X.D., Cohen, B., Bi, S.J., Zhao, X.F., and Selby, D., 2014, Longevity of magmatic–hydrothermal systems in the Daye Cu-Fe-Au District, eastern China with implications for mineral exploration: Ore Geology Reviews, v. 57, p. 375–392.
Li, S., Suo, Y., Li, X., Zhou, J., Santosh, M., Wang, P., Wang, G., Guo, L., Yu, S., and Lan, H., 2019, Mesozoic tectono-magmatic response in the East Asian ocean-continent connection zone to subduction of the Paleo-Pacific Plate: Earth-Science Reviews, v. 192, p. 91–137.
Li, W., and Costa, F., 2020, A thermodynamic model for F-Cl-OH partitioning between silicate melts and apatite including non-ideal mixing with application to constraining melt volatile budgets: Geochimica et Cosmochimica Acta, v. 269, p. 203–222.
Li, W., Audétat, A., and Zhang, J., 2015, The role of evaporites in the formation of magnetite-apatite deposits along the Middle and Lower Yangtze River, China: Evidence from LA-ICP-MS analysis of fluid inclusions: Ore Geology Reviews, v. 67, p. 264–278.
Li, Y.M., Wang, X.G., Li, J.M., Zeng, Q.Q., Hu, Z.H., Wang, D.L., and Wang, M.S., 2015, Discussion on the geological characteristics of Baoshan Cu polymetallic deposit and its genesis in Jiujiang-Ruichang ore concentration, Jiangxi province: Geological Survey and Research, v. 38, p. 256–264 (in Chinese with English abstract).
Li, Z.X., and Li, X.H., 2007, Formation of the 1300-km-wide intracontinental orogen and postorogenic magmatic province in Mesozoic South China: A flat-slab subduction model: Geology, v. 35, p. 179.
Ling, M.X., Wang, F.Y., Ding, X., Hu, Y.H., Zhou, J.B., Zartman, R.E., Yang, X.Y., and Sun, W.D., 2009, Cretaceous ridge subduction along the lower Yangtze River belt, eastern China: Economic Geology, v. 104, p. 303–321.
Liu, L., Gurnis, M., Seton, M., Saleeby, J., Müller, R.D., and Jackson, J.M., 2010, The role of oceanic plateau subduction in the Laramide orogeny: Nature Geoscience, v. 3, p. 353–357.
Liu, L., Peng, D., Liu, L., Chen, L., Li, S., Wang, Y., Cao, Z., and Feng, M., 2021, East Asian lithospheric evolution dictated by multistage Mesozoic flat-slab subduction: Earth-Science Reviews, v. 217, article 103621.
Liu, S.A., Li, S.G., He, Y.S., and Huang, F., 2010, Geochemical contrasts between early Cretaceous ore-bearing and ore-barren high-Mg adakites in central-eastern China: Implications for petrogenesis and Cu-Au mineralization: Geochimica et Cosmochimica Acta, v. 74, p. 7160–7178.
Liu, Y., Hu, Z., Zong, K., Gao, C., Gao, S., Xu, J., and Chen, H., 2010, Reappraisement and refinement of zircon U-Pb isotope and trace element analyses by LA-ICP-MS: Chinese Science Bulletin, v. 55, p. 1535–1546.
Lü, Q., Meng, G., Zhang, K., Liu, Z., Yan, J., Shi, D., Han, J., and Gong, X., 2021, The lithospheric architecture of the Lower Yangtze metallogenic belt, east China: Insights into an extensive Fe-Cu mineral system: Ore Geology Reviews, v. 132, article 103989.
Loucks, R.R., 2021, Deep entrapment of buoyant magmas by orogenic tectonic stress: Its role in producing continental crust, adakites, and porphyry copper deposits: Earth-Science Reviews, v. 220, article 103744.

Loucks, R.R., Fiorentini, M.L., and Henríquez, G.J., 2020, New magmatic oxybarometer using trace elements in zircon: Journal of Petrology, v. 61, p. 1–30.

Lu, Y.J., 2016, Zircon compositions as a pathfinder for porphyry Cu ± Mo ± Au deposits: Society of Economic Geologists, Special Publication 19, p. 329–347.

Ludwig, K.R., 2012, User's manual for Isoplot version 3.75–4.15: A geochronological toolkit for Microsoft Excel: Berkeley Geochronological Center, Special Publication no. 5, 75 p.

Luo, G., Zhang, Z., Du, Y., Pang, Z., Zhang, Y., and Jiang, Y., 2015, Origin and evolution of ore-forming fluids in the Hemushan magnetite-apatite deposit, Anhui Province, Eastern China, and their metallogenic significance: Journal of Asian Earth Sciences, v. 113, p. 1100–1116.

Ma, F., Jiang, S., Jiang, Y., Ni, P., and Ling, H., 2006, Fluid inclusions and HO isotopic compositions in the Washan and Dongshan iron deposits, Ningwu basin, China: Acta Petrologica Sinica, v. 22, p. 2581–2589 (in Chinese with English abstract).

Mao, J., Wang, Y., Lehmann, B., Yu, J., Du, A., Mei, Y., Li, Y., Zang, W., Stein, H.J., and Zhou, T., 2006, Molybdenite Re-Os and albite $^{40}Ar/^{39}Ar$ dating of Cu-Au-Mo and magnetite porphyry systems in the Yangtze River valley and metallogenic implications: Ore Geology Reviews, v. 29, p. 307–324.

Mao, J., Xie, G., Duan, C., Pirajno, F., Ishiyama, D., and Chen, Y., 2011, A tectono-genetic model for porphyry-skarn-stratabound Cu-Au-Mo-Fe and magnetite-apatite deposits along the Middle-Lower Yangtze River Valley, eastern China: Ore Geology Reviews, v. 43, p. 294–314.

Mao, J., Xiong, B., Liu, J., Pirajno, F., Cheng, Y., Ye, H., Song, S., and Dai, P., 2017, Molybdenite Re/Os dating, zircon U–Pb age and geochemistry of granitoids in the Yangchuling porphyry W-Mo deposit (Jiangnan tungsten ore belt), China: Implications for petrogenesis, mineralization and geodynamic setting: Lithos, v. 286–287, p. 35–52.

Mao, J., Liu, P., Goldfarb, R.J., Goryachev, N.A., Pirajno, F., Zheng, W., Zhou, M., Zhao, C., Xie, G., and Yuan, S., 2021, Cretaceous large-scale metal accumulation triggered by post-subductional large-scale extension, East Asia: Ore Geology Reviews, v. 136, article 104270.

Meinert, L.D., Dipple, G.M., and Nicolescu, S., 2005, World skarn deposits: Economic Geology, 100th Anniversary Volume, p. 299–336.

Meng, X., Kleinsasser, J.M., Richards, J.P., Tapster, S.R., Jugo, P.J., Simon, A.C., Kontak, D.J., Robb, L., Bybee, G.M., Marsh, J.H., and Stern, R.A., 2021a, Oxidized sulfur-rich arc magmas formed porphyry Cu deposits by 1.88 Ga: Nature Communications, v. 12, article 2189.

Meng, X., Richards, J.P., Kontak, D.J., Simon, A.C., Kleinsasser, J.M., Marsh, J.H., Stern, R.A., and Jugo, P.J., 2021b, Variable modes of formation for tonalite-trondhjemite-granodiorite-diorite (TTG)-related porphyry-type Cu ± Au deposits in the Neoarchean Southern Abitibi Subprovince (Canada): Evidence from petrochronology and oxybarometry: Journal of Petrology, v. 62, p. 1–29.

Meng, X., Simon, A.C., Kleinsasser, J.M., Mole, D.R., Kontak, D.J., Jugo, P.J., Mao, J., and Richards, J.P., 2022, Formation of oxidized sulfur-rich magmas in Neoarchaean subduction zones: Nature Geoscience, v. 15, p. 1064–1070.

Mutch, E.J.F., Blundy, J.D., Tattitch, B.C., Cooper, F.J., and Brooker, R.A., 2016, An experimental study of amphibole stability in low-pressure granitic magmas and a revised Al-in-hornblende geobarometer: Contributions to Mineralogy and Petrology, v. 171, article 85.

Nash, W.M., Smythe, D.J., and Wood, B.J., 2019, Compositional and temperature effects on sulfur speciation and solubility in silicate melts: Earth and Planetary Science Letters, v. 507, p. 187–198.

Ningwu-Research-Group, 1978, Magnetite porphyry deposits in Ningwu area: Beijing, Geological Publishing House, 196 p. (in Chinese).

Ouyang, L., Li, H., Lü, Q., Yang, Y., Li, X., Jiang, G., Zhang, G., Shi, D., Zheng, D., Sun, S., Tan, J., and Zhou, M., 2014, Crustal and uppermost mantle velocity structure and its relationship with the formation of ore districts in the Middle-Lower Yangtze River region: Earth and Planetary Science Letters, v. 408, p. 378–389.

Pan, Y., and Dong, P., 1999, The Lower Changjiang (Yangzi/Yangtze River) metallogenic belt, east central China: Intrusion- and wall rock-hosted Cu-Fe-Au, Mo, Zn, Pb, Ag deposits: Ore Geology Reviews, v. 15, p. 177–242.

Parat, F., and Holtz, F., 2004, Sulfur partitioning between apatite and melt and effect of sulfur on apatite solubility at oxidizing conditions: Contributions to Mineralogy and Petrology, v. 147, p. 201–212.

Piccoli, P., and Candela, P., 1994, Apatite in felsic rocks: A model for the estimation of initial halogen concentrations in the Bishop Tuff (Long Valley) and Tuolumne Intrusive Suite (Sierra Nevada Batholith) magmas: American Journal of Science, v. 294, p. 92–135.

Pirajno, F., and Zhou, T.F., 2015, Intracontinental porphyry and porphyry-skarn mineral systems in eastern China: Scrutiny of a special case "Made-in-China": Economic Geology, v. 110, p. 603–629.

Profeta, L., Ducea, M.N., Chapman, J.B., Paterson, S.R., Gonzales, S.M.H., Kirsch, M., Petrescu, L., and DeCelles, P.G., 2015, Quantifying crustal thickness over time in magmatic arcs: Scientific Reports, v. 5, article 17786.

Qiu, H., Lin, W., Chen, Y., and Faure, M., 2023, Jurassic-Early Cretaceous tectonic evolution of the North China craton and Yanshanian intracontinental orogeny in east Asia: New insights from a general review of stratigraphy, structures, and magmatism: Earth-Science Reviews, v. 237, article 104320.

Qiu, Y.M., Gao, S., McNaughton, N.J., Groves, D.I., and Ling, W., 2000, First evidence of >3.2 Ga continental crust in the Yangtze craton of south China and its implications for Archean crustal evolution and Phanerozoic tectonics: Geology, v. 28, p. 11–14.

Rasmussen, D.J., Plank, T.A., Roman, D.C., and Zimmer, M.M., 2022, Magmatic water content controls the pre-eruptive depth of arc magmas: Science, v. 375, p. 1169–1172.

Reich, M., Simon, A.C., Barra, F., Palma, G., Hou, T., and Bilenker, L.D., 2022, Formation of iron oxide-apatite deposits: Nature Reviews Earth and Environment, v. 3, p. 758–775.

Richards, J.P., 2003, Tectono-magmatic precursors for porphyry Cu-(Mo-Au) deposit formation: Economic Geology, v. 98, p. 1515–1533.

——2011, High Sr/Y arc magmas and porphyry Cu ± Mo ± Au deposits: Just add water: Economic Geology, v. 106, p. 1075–1081.

——2015, The oxidation state, and sulfur and Cu contents of arc magmas: Implications for metallogeny: Lithos, v. 233, p. 27–45.

Richards, J.P., and Kerrich, R., 2007, Special paper: Adakite-like rocks: Their diverse origins and questionable role in metallogenesis: Economic Geology, v. 102, p. 537–576.

Richards, J.P., and Mumin, A.H., 2013a, Lithospheric fertilization and mineralization by arc magmas: Genetic links and secular differences between porphyry copper ± molybdenum ± gold and magmatic-hydrothermal iron oxide copper-gold deposits: Society of Economic Geologists, Special Publication 17, p. 277–299.

——2013b, Magmatic-hydrothermal processes within an evolving Earth: Iron oxide-copper-gold and porphyry Cu ± Mo ± Au deposits: Geology, v. 41, p. 767–770.

Richards, J.P., Spell, T., Rameh, E., Razique, A., and Fletcher, T., 2012, High Sr/Y magmas reflect arc maturity, high magmatic water content, and porphyry Cu ± Mo ± Au potential: Examples from the Tethyan arcs of central and eastern Iran and western Pakistan: Economic Geology, v. 107, p. 295–332.

Richards, J.P., López, G.P., Zhu, J.J., Creaser, R.A., Locock, A.J., and Mumin, A.H., 2017, Contrasting tectonic settings and sulfur contents of magmas associated with Cretaceous porphyry Cu ± Mo ± Au and intrusion-related iron oxide Cu-Au deposits in northern Chile: Economic Geology, v. 112, p. 295–318.

Ridolfi, F., 2021, Amp-TB2: An updated model for calcic amphibole thermobarometry: Minerals, v. 11, p. 324.

Ridolfi, F., and Renzulli, A., 2012, Calcic amphiboles in calc-alkaline and alkaline magmas: Thermobarometric and chemometric empirical equations valid up to 1,130°C and 2.2 GPa: Contributions to Mineralogy and Petrology, v. 163, p. 877–895.

Ridolfi, F., Renzulli, A., and Puerini, M., 2010, Stability and chemical equilibrium of amphibole in calc-alkaline magmas: An overview, new thermobarometric formulations and application to subduction-related volcanoes: Contributions to Mineralogy and Petrology, v. 160, p. 45–66.

Rye, R.O., 1993, The evolution of magmatic fluids in the epithermal environment; the stable isotope perspective: Economic Geology, v. 88, p. 733–752.

Samake, B., Xu, Y.M., and Jiang, S.Y., 2018, Oxygen fugacity, temperature and pressure estimation from mineral chemistry of the granodiorite porphyry from the Jilongshan Au-Cu deposit and the Baiguoshu prospecting area in SE Hubei Province: A guide for mineral exploration: Journal of Geochemical Exploration, v. 184, p. 136–149.

Schiller, D., and Finger, F., 2019, Application of Ti-in-zircon thermometry to granite studies: Problems and possible solutions: Contributions to Mineralogy and Petrology, v. 174, p. 1–16.

Shi, K., Yang, X., Du, J., Cao, J., Wan, Q., and Cai, Y., 2020, Geochemical study of Cretaceous magmatic rocks and related ores of the Hucunnan Cu-Mo deposit: Implications for petrogenesis and poly-metal mineralization in the Tongling ore-cluster region: Minerals, v. 10, p. 107.

Sillitoe, R.H., 2003, Iron oxide-copper-gold deposits: An Andean view: Mineralium Deposita, v. 38, p. 787–812.

——2010, Porphyry copper systems: Economic Geology, v. 105, p. 3–41.
Simon, A.C., Pettke, T., Candela, P.A., Piccoli, P.M., and Heinrich, C.A., 2004, Magnetite solubility and iron transport in magmatic-hydrothermal environments: Geochimica et Cosmochimica Acta, v. 68, p. 4905–4914.
Simon, A.C., Knipping, J., Reich, M., Barra, F., Deditius, A.P., Bilenker, L., and Childress, T., 2018, Kiruna-type iron oxide-apatite (IOA) and iron oxide copper-gold (IOCG) deposits form by a combination of igneous and magmatic-hydrothermal processes: Evidence from the Chilean Iron Belt: Society of Economic Geologists, Special Publication 21, p. 89–114.
Skirrow, R.G., 2022, Iron oxide copper-gold (IOCG) deposits – A review (part 1): Settings, mineralogy, ore geochemistry and classification: Ore Geology Reviews, v. 140, article 104569.
Smythe, D.J., and Brenan, J.M., 2016, Magmatic oxygen fugacity estimated using zircon-melt partitioning of cerium: Earth and Planetary Science Letters, v. 453, p. 260–266.
Stock, M.J., Humphreys, M.C.S., Smith, V.C., Isaia, R., Brooker, R.A., and Pyle, D.M., 2018, Tracking volatile behaviour in subvolcanic plumbing systems using apatite and glass: Insights into pre-eruptive processes at Campi Flegrei, Italy: Journal of Petrology, v. 59, p. 2463–2492.
Su, Z.K., Zhao, X.F., Zeng, L.P., Zhao, K.D., and Hofstra, A.H., 2019, Tourmaline boron and strontium isotope systematics reveal magmatic fluid pulses and external fluid influx in a giant iron oxide-apatite (IOA) deposit: Geochimica et Cosmochimica Acta, v. 259, p. 233–252.
Sun, S.S., and McDonough, W.F., 1989, Chemical and isotopic systematics of oceanic basalts: Implications for mantle composition and processes: Geological Society, London, Special Publication 42, p. 313–345.
Tang, M., Erdman, M., Eldridge, G., and Lee, C.T.A., 2018, The redox "filter" beneath magmatic orogens and the formation of continental crust: Science Advances, v. 4, article eaar4444.
Troll, V.R., Weis, F.A., Jonsson, E., Andersson, U.B., Majidi, S.A., Högdahl, K., Harris, C., Millet, M.A., Chinnasamy, S.S., Kooijman, E., and Nilsson, K.P., 2019, Global Fe-O isotope correlation reveals magmatic origin of Kiruna-type apatite-iron-oxide ores: Nature Communications, v. 10, p. 1712.
Ulmer, P., Kaegi, R., and Müntener, O., 2018, Experimentally derived intermediate to silica-rich arc magmas by fractional and equilibrium crystallization at 1.0 GPa: An evaluation of phase relationships, compositions, liquid lines of descent and oxygen fugacity: Journal of Petrology, v. 59, p. 11–58.
Wallace, P.J., and Edmonds, M., 2011, The sulfur budget in magmas: Evidence from melt inclusions, submarine glasses, and volcanic gas emissions: Reviews in Mineralogy and Geochemistry, v. 73, p. 215–246.
Wang, F.Y., Liu, S.A., Li, S.G., and He, Y.S., 2013, Contrasting zircon Hf-O isotopes and trace elements between ore-bearing and ore-barren adakitic rocks in central-eastern China: Implications for genetic relation to Cu-Au mineralization: Lithos, v. 156, p. 97–111.
Wang, F.Y., Liu, S.A., Li, S., Akhtar, S., and He, Y., 2014, Zircon U-Pb ages, Hf-O isotopes and trace elements of Mesozoic high Sr/Y porphyries from Ningzhen, eastern China: Constraints on their petrogenesis, tectonic implications and Cu mineralization: Lithos, v. 200–201, p. 299–316.
Wang, J., Xie, G.Q., Yu, Z.F., Zhu, Q.Q., Li, W., and Yang, Q.Y., 2014, Geological and skarn mineral characteristics of the Jilongshan skarn Au deposit in southeastern Hubei Province: Acta Petrologica et Mineralogica, v. 33, p. 149–162.
Wang, Q., Wyman, D., Xu, J.F., Zhao, Z.H., Jian, P., and Zi, F., 2007, Partial melting of thickened or delaminated lower crust in the middle of eastern China: Implications for Cu-Au mineralization: The Journal of Geology, v. 115, p. 149–161.
Wang, S.W., Zhou, T.F., Yuan, F., Fan, Y., Zhang, L.J., and Song, Y.L., 2015, Petrogenesis of Dongguashan skarn-porphyry Cu-Au deposit related intrusion in the Tongling district, eastern China: Geochronological, mineralogical, geochemical and Hf isotopic evidence: Ore Geology Reviews, v. 64, p. 53–70.
Wang, S.W., Zhou, T., Yuan, F., Fan, Y., Cooke, D.R., Zhang, L., Fu, B., and White, N.C., 2016, Geochemical characteristics of the Shujiadian Cu deposit related intrusion in Tongling: Petrogenesis and implications for the formation of porphyry Cu systems in the Middle-Lower Yangtze River Valley metallogenic belt, eastern China: Lithos, v. 252–253, p. 185–199.
Watanabe, T., Koyaguchi, T., and Seno, T., 1999, Tectonic stress controls on ascent and emplacement of magmas: Journal of Volcanology and Geothermal Research, v. 91, p. 65–78.
Webster, J.D., Tappen, C.M., and Mandeville, C.W., 2009, Partitioning behavior of chlorine and fluorine in the system apatite-melt-fluid. II: Felsic silicate systems at 200MPa: Geochimica et Cosmochimica Acta, v. 73, p. 559–581.
Wen, C.H., Shao, Y.J., Li, B., Dick, J.M., Lai, J.Q., Huang, G.F., and Luo, X.Y., 2019, Fluid evolution of the Wushan skarn-dominant copper deposit in the Middle-Lower Yangtze River metallogenic belt, eastern China: Ore Geology Reviews, v. 112, article 103035.
Wen, G., Zhou, R.J., Li, J.W., Chang, J., Hu, H., Yan, D.R., Wei, K.T., and Jin, S.G., 2020, Skarn metallogeny through zircon record: An example from the Daye Cu-Au-Fe-Mo district, eastern China: Lithos, v. 378–379, article 105807.
Wendt, I., and Carl, C., 1991, The statistical distribution of the mean squared weighted deviation: Chemical Geology: Isotope Geoscience section, v. 86, p. 275–285.
Wu, F.Y., Ji, W.Q., Sun, D.H., Yang, Y.H., and Li, X.H., 2012, Zircon U-Pb geochronology and Hf isotopic compositions of the Mesozoic granites in southern Anhui Province, China: Lithos, v. 150, p. 6–25.
Wu, F.Y., Yang, J.H., Xu, Y.G., Wilde, S.A., and Walker, R. J., 2019, Destruction of the North China craton in the Mesozoic: Annual Review of Earth and Planetary Sciences, v. 47, p. 173–195.
Wu, M.A., Wang, Q.S., Zheng, G.W., Cai, X.B., Yang, S.X., and Di, Q.S., 2011, Discovery of the Nihe iron deposit in Lujiang, Anhui, and its exploration significance: Acta Geologica Sinica, v. 85, p. 802–809 (in Chinese with English abstract).
Xu, Y.M., Jiang, S.Y., Zhu, Z.Y., and Zhou, W., 2015, Mineral chemistry and H-O-S-Pb isotopic compositions of skarn type copper deposits in the Jiurui district of the Middle-Lower Yangtze River metallogenic belt, eastern China: Ore Geology Reviews, v. 69, p. 88–103.
Yan, J., Liu, J., Li, Q., Xing, G., Liu, X., Xie, J., Chu, X., and Chen, Z., 2015, In situ zircon Hf-O isotopic analyses of late Mesozoic magmatic rocks in the Lower Yangtze River belt, central eastern China: Implications for petrogenesis and geodynamic evolution: Lithos, v. 227, p. 57–76.
Yan, J., Liu, X., Wang, S., Xie, J., and Liu, J., 2021, Metallogenic type controlled by magma source and tectonic regime: Geochemical comparisons of Mesozoic magmatism between the Middle–Lower Yangtze River belt and the Dabie orogen, eastern China: Ore Geology Reviews, v. 133, article 104095.
Yan, Z., Chen, L., Xiong, X., Wang, K., Xie, R., and Hsu, H.T., 2020, Observations and modeling of flat subduction and its geological effects: Science China Earth Sciences, v. 63, p. 1069–1091.
Yang, D., Lv, Q., Yang, Z., Yan, J., XinXiong, and Chen, Y., 2021, Zircon Hf-isotopic mapping of Middle-Lower Yangtze River Valley metallogenic belt, China: Constraints on crustal properties and ore cluster formation: Lithos, v. 406–407, article 106526.
Yang, Y.Z., Chen, F., Siebel, W., Zhang, H., Long, Q., He, J.F., Hou, Z.H., and Zhu, X.Y., 2014a, Age and composition of Cu-Au related rocks from the lower Yangtze River belt: Constraints on paleo-Pacific slab roll-back beneath eastern China: Lithos, v. 202, p. 331–346.
Yang, Y.Z., Long, Q., Siebel, W., Cheng, T., Hou, Z.H., and Chen, F., 2014b, Paleo-Pacific subduction in the interior of eastern China: Evidence from adakitic rocks in the Edong-Jiurui district: The Journal of Geology, v. 122, p. 77–97.
Yang, Z.M., and Cooke, D., 2019, Porphyry copper deposits in China: Society of Economic Geologists, Special Publications 22, p. 133–187.
Yao, J., Shu, L., and Santosh, M., 2014, Neoproterozoic arc-trench system and breakup of the South China craton: Constraints from N-MORB type and arc-related mafic rocks, and anorogenic granite in the Jiangnan orogenic belt: Precambrian Research, v. 247, p. 187–207.
Yin, C.N., Xing, S.W., and Xiao, K.Y., 2016, Metallogenic characteristics and resource potential analysis of the Middle-Lower Yangtze River Fe-Cu-Au-Pb-Zn metallogenic belt: Acta Geologica Sinica, v. 90, p. 1525–1536.
Yuan, F., Zhou, T., Liu, J., Fan, Y., Cooke, D.R., and Jowitt, S.M., 2011, Petrogenesis of volcanic and intrusive rocks of the Zhuanqiao stage, Luzong basin, Yangtze metallogenic belt, east China: Implications for ore deposition: International Geology Review, v. 53, p. 526–541.
Zajacz, Z., Halter, W.E., Pettke, T., and Guillong, M., 2008, Determination of fluid/melt partition coefficients by LA-ICPMS analysis of co-existing fluid and silicate melt inclusions: Controls on element partitioning: Geochimica et Cosmochimica Acta, v. 72, p. 2169–2197.
Zeng, L.P., Zhao, X.F., Li, X.C., Hu, H., and McFarlane, C., 2016, In situ elemental and isotopic analysis of fluorapatite from the Taocun magnetite-apatite deposit, Eastern China: Constraints on fluid metasomatism: American Mineralogist, v. 101, p. 2468–2483.
Zeng, L.P., Zhao, X.F., Spandler, C., Hu, H., Hu, B., Li, J.W., and Hu, Y., 2022, Origin of high-Ti magnetite in magmatic-hydrothermal systems: Evidence from iron oxide-apatite (IOA) deposits of eastern China: Economic Geology, v. 117, p. 923–942.

Zhai, Y.S., Yao, S.Z., and Lin, X.D., 1992, Regularities of metallogenesis for copper (gold) deposits in the middle-lower reaches of the Yangtze River area: Beijing, Geological Publishing House, 120 p. (In Chinese).

Zhang, C., Li, X., Behrens, H., and Holtz, F., 2022a, Partitioning of OH-F-Cl between biotite and silicate melt: Experiments and an empirical model: Geochimica et Cosmochimica Acta, v. 317, p. 155–179.

Zhang, F., Williamson, B.J., Rollinson, G.K., and Hughes, H.S.R., 2023, A mineralogical investigation into the formation of ore-barren endoskarn: An example from the Tonglushan porphyry system, eastern China: Ore Geology Reviews, v. 157, article 105441.

Zhang, J., Liu, L., Yu, Z., Yang, X., Liu, Z., and Li, H., 2021, Petrogenesis and metallogeny of the Dongguashan Cu-Au deposit in the Tongling ore-cluster region, the Lower Yangtze River metallogenic belt: Constraints from geochemistry and geochronology: Geochemistry, v. 81, article 125822.

Zhang, J.B., Wang, R., and Hong, J., 2022b, Amphibole fractionation and its potential redox effect on arc crust: Evidence from the Kohistan arc cumulates: American Mineralogist, v. 107, p. 1779–1788.

Zhang, S., Ma, Q., Chen, H., Long, X., Chu, G., Cheng, J., Xia, X., and Li, R., 2021, Precambrian crust growth and reworking of the eastern Yangtze Craton: Insights from xenocrystic zircons in the lamprophyres from the Middle-Lower Yangtze belt, China: Precambrian Research, v. 355, article 106121.

Zhang, S., Wu, M.A., Zhao, W.G., Zhang, Y.Y., Li, X.D., and Wang, J., 2014, Geochemistry characteristics of Nihe iron deposit in Lujiang, Anhui province and their constraints to ore genesis: Acta Petrologica Sinica, v. 30, p. 1382–1396 (in Chinese with English abstract).

Zhang, Y., Chen, H., Cheng, J., Tian, J., Zhang, L., and Olin, P., 2022, Pyrite geochemistry and its implications on Au-Cu skarn metallogeny: An example from the Jiguanzui deposit, eastern China: American Mineralogist, v. 107, p. 1910–1925.

Zhang, Y., Cheng, J., Tian, J., Pan, J., Sun, S., Zhang, L., Zhang, S., Chu, G., Zhao, Y., and Lai, C., 2019, Texture and trace element geochemistry of quartz in skarn system: Perspective from Jiguanzui Cu-Au skarn deposit, eastern China: Ore Geology Reviews, v. 109, p. 535–544.

Zhang, Z., Du, Y., and Zhang, J., 2013, Alteration, mineralization, and genesis of the zoned Tongshan skarn-type copper deposit, Anhui, China: Ore Geology Reviews, v. 53, p. 489–503.

Zhang, Z., Ling, M., Lin, W., Sun, M., and Sun, W., 2020, "Yanshanian Movement" induced by the westward subduction of the paleo-Pacific plate: Solid Earth Sciences, v. 5, p. 103–114.

Zhao, X.F., Zeng, L.P., Liao, W., Li, W.T., Hu, H., and Li, J.W., 2020, An overview of recent advances in porphyrite iron (iron oxide-apatite, IOA) deposits in the Middle-Lower Yangtze River Valley metallogenic belt and its implication for ore genesis: Earth Science Frontiers, v. 27, p. 197–217 (In Chinese with English abstract).

Zhao, Y., Zhang, Y., and Bi, C., 1999, Geology of gold-bearing skarn deposits in the middle and lower Yangtze River Valley and adjacent regions: Ore Geology Reviews, v. 14, p. 227–249.

Zheng, P., and Wen, C.H., 2017, Fluid inclusion evidence for the Hucun copper ore deposit in Tongling area of Anhui province: Acta Petrologica et Mineralogica, v. 36, p. 564–580 (in Chinese with English abstract).

Zheng, Y.F., Xiao, W.J., and Zhao, G., 2013, Introduction to tectonics of China: Gondwana Research, v. 23, p. 1189–1206.

Zhou, M.F., Yan, D.P., Kennedy, A.K., Li, Y.Q., and Ding, J., 2002, SHRIMP U-Pb zircon geochronological and geochemical evidence for Neoproterozoic arc-magmatism along the western margin of the Yangtze Block, South China: Earth and Planetary Science Letters, v. 196, p. 51–67.

Zhou, T., Yuan, F., Yue, S., Liu, X., Zhang, X., and Fan, Y., 2007, Geochemistry and evolution of ore-forming fluids of the Yueshan Cu-Au skarn-and vein-type deposits, Anhui Province, South China: Ore Geology Reviews, v. 31, p. 279–303.

Zhou, T., Fan, Y., Yuan, F., Zhang, L., Qian, B., Ma, L., and Yang, X., 2013, Geology and geochronology of magnetite-apatite deposits in the Ning-Wu volcanic basin, eastern China: Journal of Asian Earth Sciences, v. 66, p. 90–107.

Zhou, T., Wang, S., Fan, Y., Yuan, F., Zhang, D., and White, N.C., 2015, A review of the intracontinental porphyry deposits in the Middle-Lower Yangtze River Valley metallogenic belt, Eastern China: Ore Geology Reviews, v. 65, p. 433–456.

Zhu, R., and Xu, Y., 2019, The subduction of the west Pacific plate and the destruction of the North China craton: Science China: Earth Sciences, v. 62, p. 1340–1350.

Zhu, Z.Y., Jiang, S.Y., Hu, J., Gu, L.X., and Li, J., 2014, Geochronology, geochemistry, and mineralization of the granodiorite porphyry hosting the Matou Cu-Mo (±W) deposit, Lower Yangtze River metallogenic belt, eastern China: Journal of Asian Earth Sciences, v. 79, p. 623–640.

Xuyang Meng is a full professor at the China University of Geosciences (Beijing) in China. He started his Ph.D. program at the University of Alberta, and received the Ph.D. degree from Laurentian University in 2021, followed by a one-year postdoctoral study at the University of Michigan (Ann Arbor). His research focuses on the metallogeny of magmatic-hydrothermal deposits using a variety of geologic and geochemical tools including field mapping, oxybarometry, thermobarometry, EMPA, LA-ICP-MS, SIMS, and μ-XANES. He has conducted research on Archean to Miocene magmatic-hydrothermal Cu ± Au ± Fe deposits in China, Canada, Namibia, Serbia, and South America.